



저작자표시-비영리-변경금지 2.0 대한민국

이용자는 아래의 조건을 따르는 경우에 한하여 자유롭게

- 이 저작물을 복제, 배포, 전송, 전시, 공연 및 방송할 수 있습니다.

다음과 같은 조건을 따라야 합니다:



저작자표시. 귀하는 원저작자를 표시하여야 합니다.



비영리. 귀하는 이 저작물을 영리 목적으로 이용할 수 없습니다.



변경금지. 귀하는 이 저작물을 개작, 변형 또는 가공할 수 없습니다.

- 귀하는, 이 저작물의 재이용이나 배포의 경우, 이 저작물에 적용된 이용허락조건을 명확하게 나타내어야 합니다.
- 저작권자로부터 별도의 허가를 받으면 이러한 조건들은 적용되지 않습니다.

저작권법에 따른 이용자의 권리는 위의 내용에 의하여 영향을 받지 않습니다.

이것은 [이용허락규약\(Legal Code\)](#)을 이해하기 쉽게 요약한 것입니다.

[Disclaimer](#)

**Ph.D. DISSERTATION**

**Synthesis and Photoelectrochemical Analysis  
of Metal Oxide Semiconductor  
Heteronanostructures  
for Efficient Water Splitting Photoanodes**

고효율 물분해 광전극 개발을 위한

금속 산화물 반도체 이종접합 나노구조체 합성 및 광전기화학적 특성 연구

**By**

**Bo Reum Lee**

**February 2021**

**DEPARTMENT OF MATERIALS SCIENCE AND ENGINEERING**

**COLLEGE OF ENGINEERING**

**SEOUL NATIONAL UNIVERSITY**

# Synthesis and Photoelectrochemical Analysis of Metal Oxide Semiconductor Heteronanostructures for Efficient Water Splitting Photoanodes

Advisor: Prof. Ho Won Jang

by

Bo Reum Lee

A thesis submitted to the Graduate Faculty of Seoul National University  
in partial fulfillment of the requirements  
for the Degree of Doctor of Philosophy  
Department of Materials Science and Engineering

December 2020

Approved

by

Chairman of Advisory Committee: Jin Young Kim

Vice-Chairman of Advisory Committee: Ho Won Jang

Advisory Committee: Jeong-Yun Sun

Advisory Committee: Soo Young Kim

Advisory Committee: Sanghan Lee



## **Abstract**

---

As the global energy demand grows, the development of clean and sustainable energy production technique has been regarded as one of the most significant issue presently. In this regard, photoelectrochemical (PEC) water splitting, which converts solar energy directly to chemical energy, is one of the most promising candidates for clean and efficient energy technology that can be an alternative of the conventional energy, fossil fuels. There have been numerous efforts to obtain the efficient and stable PEC electrodes using semiconductors, however, the solar-to-hydrogen (STH) efficiency through PEC water splitting is far below the theoretical value. To thoroughly replace the conventional energy, more efforts on the development of photoelectrodes should be devoted.

This thesis contains various approaches to obtain efficient water splitting semiconductor photoelectrodes. Especially, the development of photoanodes would be discussed since the water oxidation rate determines the overall water splitting reaction. Firstly, in chapter 1, the principles of PEC water splitting are described and the challenges to overcome the limitations of semiconductors as photoelectrodes are introduced. Constructing type II heterojunction and nanostructure morphology control are the vital ways for

photoelectrodes. Additionally, passivation, co-catalyst deposition, and metal ion doping can be the effective way to promote photocatalytic reactions.

In chapter 2, facile all-solution process to fabricated  $\text{WO}_3/\text{BiVO}_4$  heteronanostructures would be introduced. Because the ultimate goal is to produce sustainable energy, it is required to use sustainable process. Hydrothermal method was used to synthesis vertically grown  $\text{WO}_3$  nanorods on the FTO substrate with the precise morphology control. After that,  $\text{BiVO}_4$  thin layer was deposited on the  $\text{WO}_3$  nanorods by pulsed-electrodeposition. The optimized  $\text{WO}_3/\text{BiVO}_4$  heteronanostructures exhibit the high photocurrent density which is double that of pristine  $\text{WO}_3$  photoanode. The photostability was also enhanced despite the natural instability of  $\text{BiVO}_4$ . The improvement on the PEC properties of the photoanodes is attributed to its core-shell nanostructures. Pulsed-electrodeposition enabled the thin and conformal coating of  $\text{BiVO}_4$  on  $\text{WO}_3$  nanorods resulting in the efficient charge transfer and charge separation. Moreover, the core-shell nanostructures allowed the photoanodes to exhibit higher photocurrent density under front illumination.

In chapter 3,  $\beta\text{-In}_2\text{S}_3$ -based photoanodes with narrow band gap of around 2.1 eV is introduced. Owing to its unique crystal structures,  $\text{In}_2\text{S}_3$  has attracted renewed attention as photoanodes recently. Various strategies were integrated to enhance PEC properties of the  $\text{In}_2\text{S}_3$ -based photoanodes. First of all, the

$\text{In}_2\text{O}_3/\text{In}_2\text{S}_3$  heteronanostructures were synthesized by glancing angle deposition and chemical bath deposition for  $\text{In}_2\text{O}_3$  nanorods and  $\text{In}_2\text{S}_3$  nanosheets, respectively. Due to the controlled morphology and the formation of type II heterostructures, the photocurrent density was enhanced and onset potential was negatively shifted. In addition, cobalt (Co) ions were doped into  $\text{In}_2\text{S}_3$  layer by simply adding Co precursor powder in the bath solution. The resultant photoanodes with different doping concentration showed improved PEC properties including light absorption and charge transfer efficiency. These factors could prevent the hole accumulation and finally, contributed to enhance the photostability as well as the photocurrent density of the  $\beta\text{-In}_2\text{S}_3$ -based photoanodes.

**Keywords:** Photoelectrochemical (PEC), Water splitting, Heterostructure, Core-Shell, Photostability

**Student ID:** 2014-21436

**Bo Reum Lee**

## Table of Contents

---

Abstract .....	1
Table of Contents.....	4
List of Tables.....	7
List of Figures .....	8
Chapter 1 .....	14
Photoelectrochemical Water Splitting .....	14
1.1. Introduction .....	15
1.2. PEC Water Splitting.....	16
1.2.1. Principles of PEC Water Splitting .....	17
1.2.2. Determining Factors for PEC Water Splitting Efficiencies .....	21
1.3. Semiconductor Materials for Solar Water Splitting .....	22
1.3.1. Band-Edge Positions.....	22
1.3.2. Narrow-Gap Materials and Corrosion Level.....	24
1.4. Various Strategies to Enhance PEC Properties of $\text{In}_2\text{S}_3$ .....	27
1.4.1. Nanostructure Morphology Control.....	27
1.4.2. Heterostructures .....	27
1.4.3. Co-catalysts .....	28
1.4.4. Surface Modification and Passivation .....	28
1.4.5. Doping.....	28

1.5. Scope and Objectives of the Thesis .....	29
1.6. References.....	32
Chapter 2.....	35
All-Solution-Processed WO <sub>3</sub> /BiVO <sub>4</sub> Core–Shell Nanorod Arrays for Highly Stable Photoanodes .....	35
2.1. Introduction .....	36
2.2. Experimental Details .....	40
2.2.1. Synthesis of the WO <sub>3</sub> Nanorod Array .....	40
2.2.2. Preparation of WO <sub>3</sub> /BiVO <sub>4</sub> Heterojunction Photoanodes....	41
2.2.3. Material Characterization .....	41
2.2.4. PEC Measurements .....	42
2.3. Results and discussion .....	44
2.4. Conclusions.....	71
2.5. References.....	72
Chapter 3.....	84
Co-doped In <sub>2</sub> S <sub>3</sub> /In <sub>2</sub> O <sub>3</sub> Photoanodes for Efficient Photoelectrochemical Water Splitting.....	84
3.1. Introduction .....	85
3.1.1. Crystal Structures of In <sub>2</sub> S <sub>3</sub> .....	86
3.1.2. In <sub>2</sub> S <sub>3</sub> : Promising Material for Photoelectrodes .....	87
3.1.3. Limitations of In <sub>2</sub> S <sub>3</sub> as Photoelectrodes.....	89

<b>3.3. Experimental Details .....</b>	<b>91</b>
<b>3.3.1. Preparation of In<sub>2</sub>O<sub>3</sub> Nanorods .....</b>	<b>91</b>
<b>3.3.2. Preparation of In<sub>2</sub>O<sub>3</sub>/In<sub>2</sub>S<sub>3</sub> and In<sub>2</sub>O<sub>3</sub>/Co Doped In<sub>2</sub>S<sub>3</sub>     Heterostructures .....</b>	<b>92</b>
<b>3.3.3. Characterization .....</b>	<b>92</b>
<b>3.3.4. PEC Measurement.....</b>	<b>93</b>
<b>3.4. Results and Discussion .....</b>	<b>96</b>
<b>3.5. Conclusions.....</b>	<b>107</b>
<b>3.6. References.....</b>	<b>108</b>
<b>4. Conclusions .....</b>	<b>118</b>
<b>Abstract (in Korean) .....</b>	<b>120</b>

## List of Tables

---

<b>Table 2.1</b> Fitted series resistance ( $R_s$ ) and charge transfer resistance ( $R_{ct}$ ) across the electrolyte/anode interface of pristine $WO_3$ nanorods synthesized at different temperature. ....	<b>46</b>
<b>Table 2.2</b> PEC performance of the reported $WO_3$ photoanodes. ....	<b>50</b>
<b>Table 2.3</b> Flat band potential and donor density for $WO_3$ and $WO_3/9-BVO$ anodes. ....	<b>59</b>
<b>Table 2.4</b> PEC performance of the reported $WO_3/BiVO_4$ photoanodes. ....	<b>70</b>

## List of Figures

---

<b>Figure 1.1</b> Hydrogen evolution reaction (HER) and oxygen evolution reaction (OER) for overall water splitting with an ideal semiconductor material under illumination. ....	<b>18</b>
<b>Figure 1.2</b> Schematics of PEC water splitting using (a) a photoanode and a counter cathode, (b) a photocathode and a counter anode, and (c) series-connected photoanode and photocathode. Republished with permission of Royal Society of Chemistry, from [6]. ....	<b>19</b>
<b>Figure 1.3</b> (a) Band edge positions of several semiconductor materials using the normal hydrogen electrode (NHE) as a reference. (b) Electromagnetic wave spectrum and absorbable wave range of each semiconductor. ....	<b>23</b>
<b>Figure 1.4</b> Calculated oxidation and reduction potentials ( $\Phi_{ox}$ as red bars and $\Phi_{re}$ as black bars) relative to the NHE and vacuum level for some semiconductors in solution at pH = 0, the ambient temperature 298.15 K, and pressure 1 bar. Reprinted with permission from [8] Copyright (2012) American Chemical Society. ....	<b>26</b>
<b>Figure 1.5</b> Various strategies to overcome the limitations and to improve PEC properties of semiconductor photoanodes. ....	<b>31</b>
<b>Figure 2.1</b> Schematic illustration of $WO_3/BiVO_4$ nanostructured photoanode fabrication. ....	<b>39</b>

**Figure 2.2** (a) Photographic images of WO<sub>3</sub> anodes synthesized at different temperatures. SEM images of WO<sub>3</sub> nanorods synthesized at (b) 120, (c) 140, (d) 160, (e) 170, and (f) 180 °C for 4 h. The insets are the cross-sectional view of nanorods on FTO.....**43**

**Figure 2.3** Cross-section SEM images of hydrothermally synthesized WO<sub>3</sub> at 170 °C for 30 minutes.....**45**

**Figure 2.4** (a) Linear sweep voltammograms tested at a scan rate of 10 mV/s under AM 1.5 G solar light, (b) electrochemical impedance spectra measured at 0.6 V vs. Ag/AgCl, and (c) incident photon-to-current efficiency data at 0.6 V vs. Ag/AgCl for pristine WO<sub>3</sub> nanorods synthesized at different temperature. Inset shows equivalent circuits for all WO<sub>3</sub> nanorods. All measurements were carried in 0.5 M phosphate buffer (pH 7) with 1 M Na<sub>2</sub>SO<sub>3</sub>. .....**46**

**Figure 2.6** Linear sweep voltammograms of pristine WO<sub>3</sub> anodes synthesized for different time tested in 0.5 M phosphate buffer (pH 7) with 1 M Na<sub>2</sub>SO<sub>3</sub> at a scan rate of 10 mV/s under AM 1.5 G solar light. ....**48**

**Figure 2.5** (a) Linear sweep voltammogram and (b) incident photon-to-current efficiency data of pristine WO<sub>3</sub> anodes synthesized at 180 °C tested in 0.5 M phosphate buffer (pH 7) with 1 M Na<sub>2</sub>SO<sub>3</sub> at a scan rate of 10 mV/s under AM 1.5 G solar light. ....**48**

**Figure 2.7** Linear sweep voltammograms of pristine  $\text{WO}_3$  anodes synthesized with the solution of different W concentration tested in 0.5 M phosphate buffer (pH 7) with 1 M  $\text{Na}_2\text{SO}_3$  at a scan rate of 10 mV/s under AM 1.5 G solar light. ....49

**Figure 2.8** Cross-section SEM images of  $\text{WO}_3/\text{BVO}$  heterojunction nanostructures, in which  $\text{BiVO}_4$  were formed by (a) 3, (b) 6, and (c) 9 cycles of pulsed electrodeposition on optimum  $\text{WO}_3$  nanorods synthesized by hydrothermal method.....52

**Figure 2.9** (a) TEM image of a  $\text{WO}_3/9\text{-BVO}$  nanorod and corresponding EDS element maps of (b) W, (c) Bi, (d) V, and (e) O respectively. The scale bar is 100 nm for (a-e). (f) TEM image of a  $\text{WO}_3/9\text{-BVO}$  nanorod with uniform thickness of  $\text{BiVO}_4$ . (g, h) High-resolution TEM and selected area diffraction pattern (inset) showing (g) crystalline plane of (110) and (002) of monoclinic  $\text{WO}_3$  and (h) crystalline plane of (103) and (112) of monoclinic  $\text{BiVO}_4$ . (i) X-ray diffraction patterns of pristine  $\text{WO}_3$  and  $\text{WO}_3/\text{BVO}$  photoanodes. ....54

**Figure 2.10** TEM image of a  $\text{WO}_3/9\text{-BVO}$  nanorod to show the formation of  $\text{BiVO}_4$  nanodots under high-energy electron beam.....56

**Figure 2.11** (a) Chopped linear sweep voltammograms with different numbers of cycles for  $\text{BiVO}_4$  deposition tested in 0.5 M phosphate buffer (pH 7) with 1 M  $\text{Na}_2\text{SO}_3$  at a scan rate of 10 mV/s under front illumination,

(b) electrochemical impedance spectra, (c) incident photon-to-current efficiency data, and (d) stability test data measured at 1.23 V vs. RHE for pristine WO<sub>3</sub> and WO<sub>3</sub>/BVO photoanodes.....57

**Figure 2.12** Mott-Schottky plots for optimized pristine WO<sub>3</sub> and WO<sub>3</sub>/9-BVO anodes measured in 0.5 M phosphate buffer (pH 7) with 1 M Na<sub>2</sub>SO<sub>3</sub>. .....58

**Figure 2.13** (a, d) Photographic top-view images and (b, e) Schematic illustrations of cross-view of samples after stability test. Linear sweep voltammogram (LSV) of (c) optimized pristine WO<sub>3</sub> and (f) WO<sub>3</sub>/9-BVO anodes at a scan rate of 10 mV/s under AM 1.5 G solar light with and without using hole scavenger. ....60

**Figure 2.14** (a) Linear sweep voltammogram (LSV) of optimized pristine WO<sub>3</sub> and WO<sub>3</sub>/9-BVO anodes tested in 0.5 M phosphate buffer (pH 7) at a scan rate of 10 mV/s under AM 1.5 G solar light and (b) charge transfer efficiency that was calculated by LSV data with and without using hole scavenger. ....63

**Figure 2.15** (a) Oxygen evolution curve and corresponding faradaic efficiency, (b) stability test data for WO<sub>3</sub>/9-BVO anode. All the measurement was carried out in 0.5 M phosphate buffer (pH 7) at 1.23 V vs. RHE under AM 1.5 G solar light. (c) The photograph of the sample that used in O<sub>2</sub> evolution test. ....64

**Figure 2.17** Linear sweep voltammograms of WO<sub>3</sub>/BVO anodes tested in 0.5 M phosphate buffer (pH 7) with 1 M Na<sub>2</sub>SO<sub>3</sub> at a scan rate of 10 mV/s under back illumination. ....66

**Figure 2.16** Absorbance spectra of optimized pristine WO<sub>3</sub> and WO<sub>3</sub>/9-BVO anodes. ....66

**Figure 2.18** Schematic illustration of produced photoanodes. (a, b) WO<sub>3</sub> nanorods synthesized by hydrothermal method for (a) 30 minutes and (b) 4 hours. (c, d) WO<sub>3</sub>/BVO hetero-nanostructure produced by hydrothermal and electrodeposition method. Pulsed electrodeposition was performed (c) 6 cycles and (d) 9 cycles. (e) Cross-section view of core-shell nanostructure. ....68

**Figure 3.1** Top and cross-section SEM images of pristine In<sub>2</sub>O<sub>3</sub> and In<sub>2</sub>O<sub>3</sub>/In<sub>2</sub>S<sub>3</sub> heterostructures grown on the FTO substrates. ....95

**Figure 3.2** (a) X-ray diffraction patterns of pristine In<sub>2</sub>O<sub>3</sub> and In<sub>2</sub>O<sub>3</sub>/In<sub>2</sub>S<sub>3</sub> photoanodes. (b) Linear sweep voltammograms of pristine In<sub>2</sub>O<sub>3</sub>, pristine In<sub>2</sub>S<sub>3</sub>, and In<sub>2</sub>O<sub>3</sub>/In<sub>2</sub>S<sub>3</sub>. Inset shows the photograph of pristine In<sub>2</sub>O<sub>3</sub>, pristine In<sub>2</sub>S<sub>3</sub>, and In<sub>2</sub>O<sub>3</sub>/In<sub>2</sub>S<sub>3</sub>.....99

**Figure 3.3** (a) TEM image of a single In<sub>2</sub>O<sub>3</sub>/Co-In<sub>2</sub>S<sub>3</sub> nanorod. (b) High-resolution TEM and (c) selected area diffraction pattern showing crystalline plane of (200) and (020) of cubic β-In<sub>2</sub>S<sub>3</sub>. ....101

**Figure 3.4** (a) TEM image of a single  $\text{In}_2\text{O}_3/\text{Co-In}_2\text{S}_3$  nanorod and corresponding EDS element maps of (b) In, (c) O, (d) S, and (e) Co respectively. ....102

**Figure 3.5** (a) Linear sweep voltammograms of pristine  $\text{In}_2\text{O}_3$ , pristine  $\text{In}_2\text{S}_3$ ,  $\text{In}_2\text{O}_3/\text{In}_2\text{S}_3$ , and  $\text{In}_2\text{O}_3/\text{Co-In}_2\text{S}_3$  with different amount of Co precursor concentration and (b) electrochemical impedance spectra of  $\text{In}_2\text{O}_3/\text{In}_2\text{S}_3$ , and  $\text{In}_2\text{O}_3/\text{Co-In}_2\text{S}_3$  with different amount of Co precursor concentration in 0.5 M  $\text{Na}_2\text{SO}_4$  solution under illumination.....104

**Figure 3.6** (a) Absorptance spectra of pristine  $\text{In}_2\text{O}_3$ ,  $\text{In}_2\text{O}_3/\text{In}_2\text{S}_3$ , and  $\text{In}_2\text{O}_3/\text{Co-In}_2\text{S}_3$  with different amount of Co precursor concentration. (b) Charge transfer efficiency of  $\text{In}_2\text{O}_3/\text{In}_2\text{S}_3$  and  $\text{In}_2\text{O}_3/\text{Co-In}_2\text{S}_3$  with different amount of Co precursor concentration that was calculated by LSV data with and without using hole scavenger.....105

# **Chapter 1**

## **Photoelectrochemical Water Splitting**

## 1.1. Introduction

The world is focusing on the sustainable energy due to the global environmental concerns and increasing demands of energy. The annual global energy consumption was 495 quadrillion British thermal units (Btu) in 2007, which is projected to be increase to 739 quadrillion Btu/year in 2035.<sup>1</sup> To replace fossil fuels which have uncertain reserves and cause air pollution, innumerable researches on sustainable energy production have been reported. Among the various renewable energy sources such as solar, wind, rain, waves, tides, and biomass, solar energy can meet the world's total energy needs with its theoretical potential of  $1.2 \times 10^5$  TW.<sup>1</sup> However, there is an enormous gap between the capability of solar energy and the actual utilization due to the high cost and limitation of technology.

Accordingly, to make good use of solar energy, it should be converted to a useful and controllable energy. Solar energy can be converted into three forms of energy: solar electricity obtained by solar cells, chemical fuel from natural or artificial photosynthesis, and solar heat.<sup>1</sup> Among them, one of the most promising pathway to utilize solar energy is hydrogen production through artificial photosynthesis. Hydrogen (H<sub>2</sub>) is a sustainable and clean energy that can be stored and transported to desired place.<sup>2</sup> There have been tremendous efforts to effectively convert abundant solar light to hydrogen energy to meet the demands. Photoelectrochemical (PEC) water splitting was proposed to

convert solar energy directly to chemical energy in the form of hydrogen by using semiconductors as light absorber.<sup>2</sup> Since Fujishima and Honda reported water splitting with titanium oxides (TiO<sub>2</sub>) for the first time in 1972, extensive efforts have been devoted to photoanodes using TiO<sub>2</sub>.<sup>3</sup> However, TiO<sub>2</sub> can only absorb the ultraviolet (UV) light because of its wide band gap of 3.2 eV, where UV light occupies only 5 % of total solar spectrum.<sup>4</sup> Hence, the semiconductor materials with the band gap energy smaller than 3.0 eV that can absorb visible light, such as tungsten oxide (WO<sub>3</sub>), bismuth vanadate (BiVO<sub>4</sub>), and hematite ( $\alpha$ -Fe<sub>2</sub>O<sub>3</sub>), also have been employed for PEC water splitting.

## **1.2. PEC Water Splitting**

PEC water splitting is an artificial photosynthesis process that uses semiconductor materials to decompose water molecules into hydrogen (H<sub>2</sub>) and oxygen (O<sub>2</sub>) gas, where H<sub>2</sub> is the simplest chemical bond. Thus, PEC water splitting is a powerful tool for the sustainable and controllable energy production. The free energy change that is needed to convert a water molecule (H<sub>2</sub>O) into H<sub>2</sub> and 1/2 O<sub>2</sub> is  $\Delta G = 237.2$  kJ/mol under standard condition which corresponds to  $\Delta E^\circ = 1.23$  eV according to the Nernst equation.<sup>5</sup>

### 1.2.1. Principles of PEC Water Splitting

As shown in Figure 1.1, the hydrogen evolution reaction (HER) and the oxygen evolution reaction (OER) can be occurred on the surface of an ideal semiconductor material with a band gap energy ( $E_g$ ) over 1.23 eV, a conduction band-edge energy ( $E_{CB}$ ) located above the electrochemical potential  $E(H^+/H_2)$ , and a valence band-edge energy ( $E_{VB}$ ) located below the electrochemical potential  $E(O_2/H_2O)$  by generating electron/hole pairs under illumination. Hence, to drive water splitting reaction on the surface of an ideal semiconductor by absorbing light, the radiant light should possess over 1.23 eV of photon energies that are equal to the wavelength shorter than 1000 nm. Once the charge carriers are photo-generated in a semiconductor, they should travel to the interface between the semiconductor and electrolyte to react with the water molecules before the charge recombination. Unfortunately, the energy losses are occurred during the charge transfer process due to the kinetic barriers at the interface. As a result, the energy of 1.6-2.4 eV is usually required for these reactions in the actual cases.

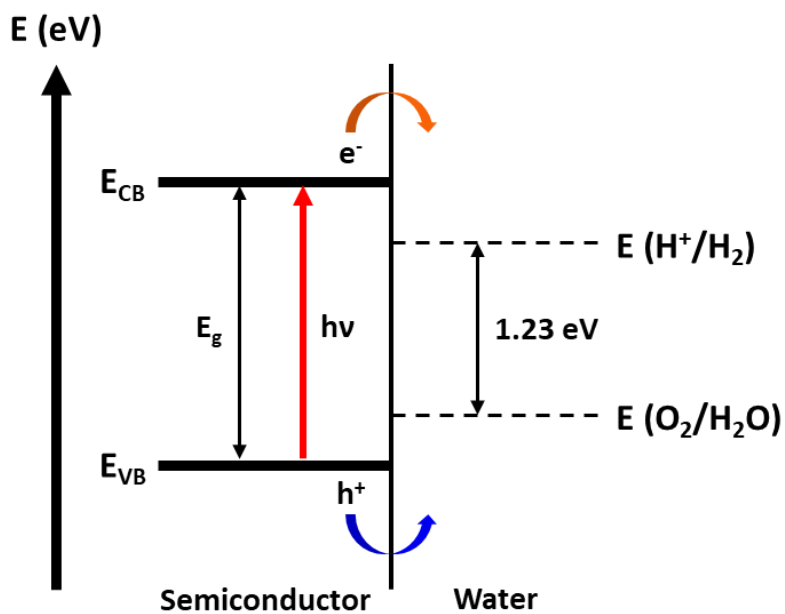
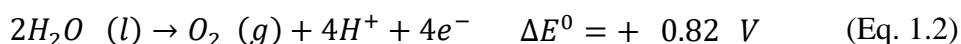


**Figure 1.1** Hydrogen evolution reaction (HER) and oxygen evolution reaction (OER) for overall water splitting with an ideal semiconductor material under illumination.

A PEC water splitting cell can be divided into a photocathode for hydrogen generation and a photoanode for oxygen generation with the following reactions:



$$\Delta G^0 = 237.2 \text{ kJ/}$$

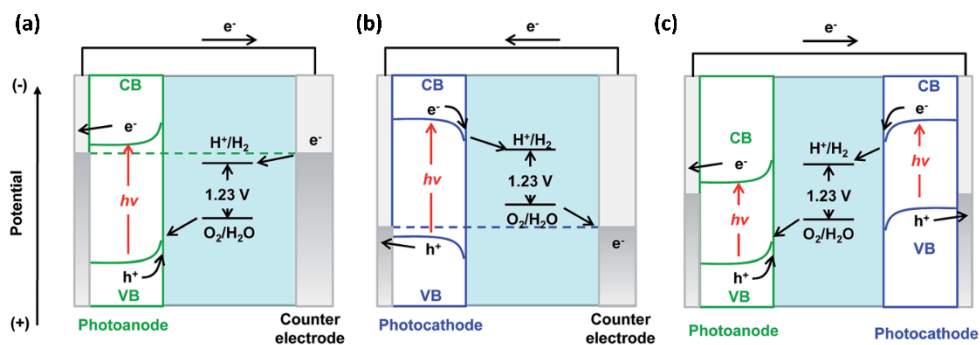


**Figure 1.2** Schematics of PEC water splitting using (a) a photoanode and a counter cathode, (b) a photocathode and a counter anode, and (c) series-connected photoanode and photocathode. Republished with permission of Royal Society of Chemistry, from [6].

A half-cell set up using a conductive material with a high catalytic activity such as platinum (Pt) as a counter electrode enables to evaluate the characteristics of the individual photoelectrode (photocathode or photoanode) as shown in Figure 1.2.<sup>6</sup>

Since the oxygen evolution reaction (OER) includes four-electron-transfer process and the hydrogen evolution reaction (HER) requires two electrons according to the equation 1.1 and 1.2, OER is the rate-determining step in an overall water splitting, that is, the development of efficient photoanodes is important.

For a typical photoanode, when the light with sufficient energy is irradiated onto the photoanode, the semiconductor absorbs the light and electron-hole pairs are produced. The electrons which jump to the conduction band travel through the material to the direction of counter electrode and reduce water molecules to produce hydrogen. At the same time, the holes left in valence band are transported to the interface of electrode/electrolyte and oxidize water molecules if the  $E_{VB}$  of the material is located below the water oxidation potential.<sup>2</sup> Since the water electrolysis in a PEC cell occurs directly at the interface between the electrodes and electrolyte, the hydrogen and oxygen can be collected separately on each electrodes.

### **1.2.2. Determining Factors for PEC Water Splitting Efficiencies**

The semiconductor photoelectrodes should satisfy mainly three factors to achieve high energy conversion efficiency: (1) sufficient light absorption, (2) efficient charge separation and transport before the photo-generated electrons and holes recombine, and (3) fast charge transfer at the interface of electrode/electrolyte to reduce (or oxidize) water molecules.<sup>7</sup> First, the light adsorption efficiency can be enhanced by choosing appropriate band position and narrow band gap materials and controlling the nanostructures of photoelectrodes. The charge separation and transport efficiency is affected by the hole diffusion length, crystallinity and carrier mobility of the materials. Constructing type II heterostructure also can facilitate the charge separation. Finally, the charge transfer efficiency can be adjusted by the surface states and resistance between electrode and electrolyte. The sluggish kinetics at the interface of electrode/electrolyte can be improved by loading co-catalyst or passivation layer.

## **1.3. Semiconductor Materials for Solar Water Splitting**

### **1.3.1. Band-Edge Positions**

As mentioned in the previous section, the band-edge positions of the material should be properly located relative to the water redox potential for water splitting and gas evolution. In detail, when the  $E_{CB}$  is located higher than the water reduction level, HER reaction would be occurred. Likewise, when the  $E_{VB}$  is located lower than the water oxidation level, OER reaction can be occurred. The band positions and band gap of several semiconductor materials are depicted in Figure 1.3a. Additionally, the charge transfer at the interface of electrode/electrolyte is active when the potential difference between  $E_{VB}$  and  $E(H_2O/O_2)$  for photoanodes and the  $E_{CB}$  and  $E(H^+/H_2)$  for photocathodes is large enough. Otherwise, the sluggish kinetics would result in the accumulation of charge carriers on the surface of the electrode.

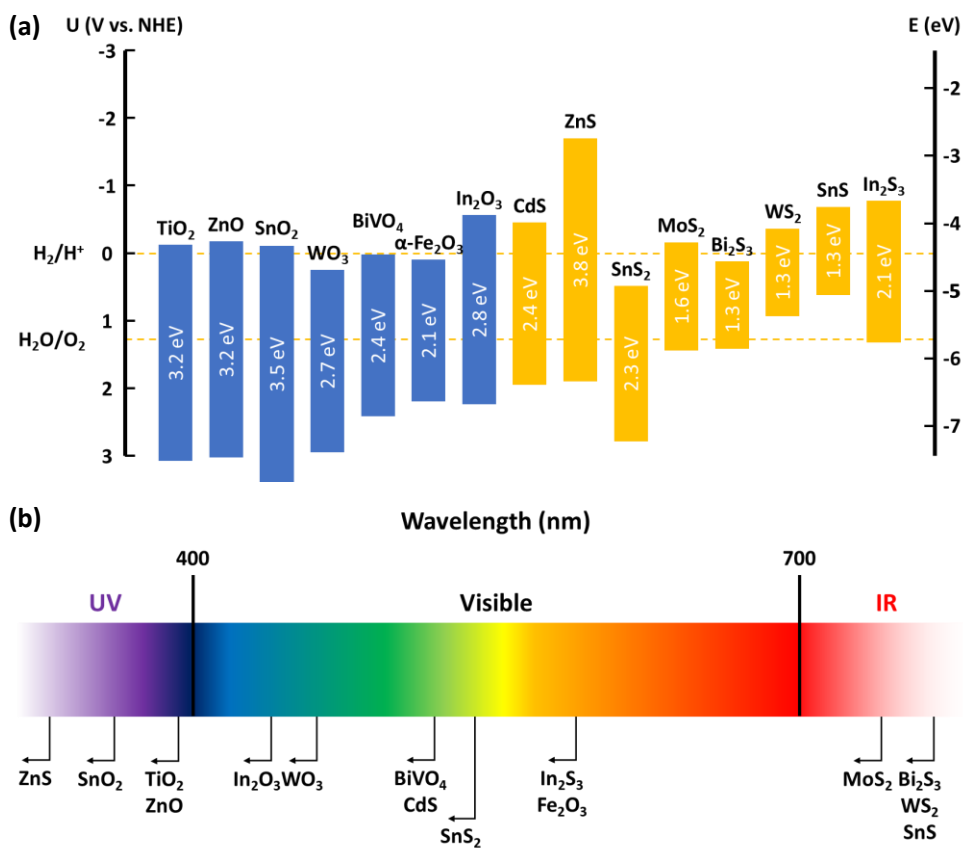


**Figure 1.3** (a) Band edge positions of several semiconductor materials using the normal hydrogen electrode (NHE) as a reference. (b) Electromagnetic wave spectrum and absorbable wave range of each semiconductor.

### 1.3.2. Narrow-Gap Materials and Corrosion Level

The theoretical maximum photocurrent is dependent on the band gap of the material. The semiconductor materials can absorb the light that possesses the energy higher than the band gap. Hence, the semiconductors with narrower band gap can absorb wider range of wavelength of the light as shown in Figure 1.3b. Moreover, solar light consists of only 5 % of UV and 43 % of visible light. Thus, using narrow-gap materials as photoelectrodes is essential for visible light harvesting. Unfortunately, however, narrow-gap materials often suffer from photocorrosion in electrolyte. According to the previous report,<sup>8</sup> the photostability of a semiconductor material in the electrolyte under illumination is dependent on the alignment of its self-oxidation potential ( $\Phi_{ox}$ ) relative to  $E(H_2O/H_2)$  and its self-reduction potential ( $\Phi_{re}$ ) relative to  $E(H^+/H_2)$ . In other words, the material can be corroded when its  $\Phi_{ox}$  is higher than  $E(H_2O/H_2)$  or  $\Phi_{re}$  is lower than  $E(H^+/H_2)$ . Calculated oxidation and reduction potentials ( $\Phi_{ox}$  and  $\Phi_{re}$ ) for some semiconductors relative to the NHE and vacuum level are depicted in Figure 1.4. In the case of  $BiVO_4$ , the theoretical maximum photocurrent is  $7.5 \text{ mA/cm}^2$  owing to its narrow band gap of 2.4 eV. However, its  $\Phi_{re}$  is lower than both  $E(H^+/H_2)$  and  $E_{CB}$ , resulting in self-reducing in the electrolyte under illumination. Also, all of nonoxide semiconductors that have narrow band gap are thermodynamically unstable because their  $\Phi_{ox}$  is higher than  $E(O_2/H_2O)$ . As mentioned above, it is

essential to use narrow-gap materials for light harvesting in spite of their instability. Therefore, to further use these narrow-gap materials as photoelectrodes commercially, the reliability should be guaranteed. There have been numerous researches to improve stability of the narrow-gap semiconductors for decades. In the next section, various strategies reported for stable narrow-gap-based photoelectrodes will be discussed.

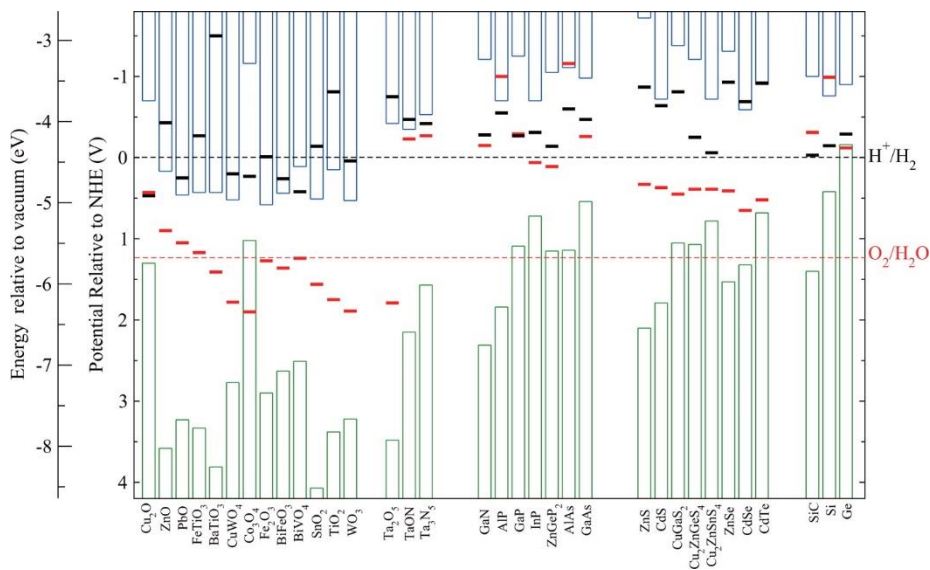


**Figure 1.4** Calculated oxidation and reduction potentials ( $\Phi_{\text{ox}}$  as red bars and  $\Phi_{\text{re}}$  as black bars) relative to the NHE and vacuum level for some semiconductors in solution at pH = 0, the ambient temperature 298.15 K, and pressure 1 bar. Reprinted with permission from [8] Copyright (2012) American Chemical Society.

## **1.4. Various Strategies to Enhance PEC Properties of In<sub>2</sub>S<sub>3</sub>**

### **1.4.1. Nanostructure Morphology Control**

Nanostructuring materials provides large surface area, abundant surface states and reaction sites compared to the bulk materials. However, the fine structural control is needed since the excessive defect sites can act as recombination sites. On the other hand, nanostructures directly grown on conductive substrates not only enlarge the interface of electrode/electrolyte for redox reactions but also trap light and collect charges efficiently and shorten minority carrier diffusion.<sup>7</sup> Also, adequate amount of active sites promotes the charge transfer at the interface resulting in high efficiency.<sup>9</sup>

### **1.4.2. Heterostructures**

The certain way to promote charge separation within the photoelectrodes is to construct type II heterostructure with appropriate band position. The photo-excited electrons and holes can immediately move to opposite direction by built-in electric field produced at the junction.<sup>10</sup> Also, constructing heterojunction with narrow band gap materials is beneficial for wide gap materials such as TiO<sub>2</sub>, In<sub>2</sub>O<sub>3</sub>, WO<sub>3</sub>, ZnO, tin oxide (SnO<sub>2</sub>) and zinc sulfide (ZnS), because of excellent ability of narrow band gap materials to absorb wide range of sunlight including visible light.

### **1.4.3. Co-catalysts**

Co-catalyst can enhance the PEC properties including the stability of photoelectrodes by capturing photo-generated carriers on the surface of the electrodes and reducing the reaction energy barrier to promote oxygen and hydrogen evolution.<sup>11</sup>

### **1.4.4. Surface Modification and Passivation**

To avoid photocorrosion and increase the stability of photoanodes which has narrow gap material as a surface material, surface treatment or passivation layer have been adopted. A passivation layer deposited on the surface of unstable materials additionally or produced by surface treatment might prevent direct contact with electrolyte and/or facilitate the transfer kinetics at the interface of electrode/electrolyte.<sup>12</sup> In addition, in the case of the additional layer material forms type II heterojunction with the inner layer, the charge separation would be far enhanced as well as the photostability. Furthermore, the electronic structure can be modified by surface treatment.<sup>9</sup>

### **1.4.5. Doping**

Doping metals into semiconductor materials induces new dopant energy levels within the band gap and the catalytic sites to promote photoelectroactivity.<sup>4</sup> When the foreign cations are inserted to the lattice,

electron density, surface defects, and trap states can be controlled to maintain the charge balance.<sup>13</sup>

## **1.5. Scope and Objectives of the Thesis**

This thesis focuses on the synthesis and control of semiconductor nanostructures to fabricate efficient and stable PEC water splitting electrodes for hydrogen production. Hydrogen energy production is one of the most promising way to utilize earth-abundant solar energy. PEC water splitting, which can convert solar energy directly to hydrogen energy, has potential to meet the global energy demands. Since the water molecules would be electrolyzed into hydrogen and oxygen by PEC electrodes using solar light, it is a clean and sustainable technique. In a thermodynamic view, the water oxidation rate determines the overall water splitting reaction since four electron and hole pairs are needed for water oxidation while the water reduction requires only two of them. Therefore, the development of the photoanodes is crucial for efficient hydrogen production by PEC water splitting. Various semiconductors with the proper band gap including metal oxides and sulfides can be used as photoanodes. Among them, narrow gap materials such as  $\text{BiVO}_4$  and  $\text{In}_2\text{S}_3$  are beneficial for photoanodes since they can absorb wide range of light including visible light. Unfortunately, these materials usually have limitations of sluggish kinetics at the interface of

electrode/electrolyte and hole accumulation resulting in the photocorrosion. To overcome the limitations and make a good use of the narrow gap materials, massive researches have been conducted as shown in Figure 1.5. In this thesis, several strategies were adopted to fabricate efficient photoanodes. One of the most essential technique for efficient water splitting is nanostructuring. Thus, various methods were used to control the morphologies of semiconductor nanostructures. Constructing of the type II heterojunction was also adopted which enables fast charge separation. Additionally, doping metal ions into the narrow gap material was conducted. After the implementation of those several strategies, deep investigation and analysis were conducted to fully understand the PEC reactions for further improvement.

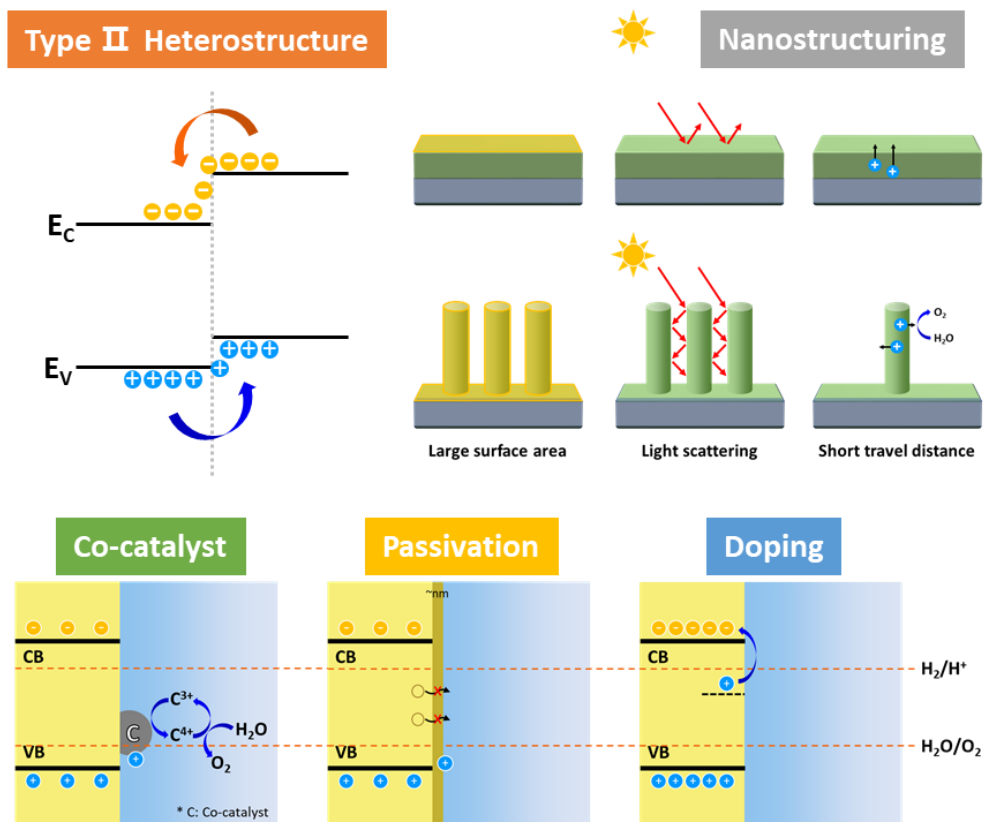


**Figure 1.5** Various strategies to overcome the limitations and to improve PEC properties of semiconductor photoanodes.

## 1.6. References

1. Zhebo Chen, H. D., Eric Miller, *Photoelectrochemical Water Splitting*. Springer: 2013.
2. Grätzel, M., Photoelectrochemical cells. *Nature* **2001**, *414*, 338-344.
3. HONDA, A. F. K., Electrochemical Photolysis of Water at a Semiconductor Electrode. *Nature* **1972**, *238*, 37-38.
4. Pulipaka, S.; Koushik, A. K. S.; Deepa, M.; Meduri, P., Enhanced photoelectrochemical activity of Co-doped  $\beta$ -In<sub>2</sub>S<sub>3</sub> nanoflakes as photoanodes for water splitting. *RSC Advances* **2019**, *9* (3), 1335-1340.
5. Michael G. Walter, E. L. W., James R. McKone, Shannon W. Boettcher, Qixi Mi, Elizabeth A. Santori, Nathan S. Lewis, Solar Water Splitting Cells. *Chemical Reviews* **2010**, *110* (11), 6446-6473.
6. Hisatomi, T.; Domen, K., Introductory lecture: sunlight-driven water splitting and carbon dioxide reduction by heterogeneous semiconductor systems as key processes in artificial photosynthesis. *Faraday Discuss* **2017**, *198*, 11-35.
7. Wang, L.; Wang, W.; Chen, Y.; Yao, L.; Zhao, X.; Shi, H.; Cao, M.; Liang, Y., Heterogeneous p-n Junction CdS/Cu<sub>2</sub>O Nanorod Arrays: Synthesis and Superior Visible-Light-Driven Photoelectrochemical Performance for Hydrogen Evolution. *ACS Appl. Mater. Interfaces* **2018**, *10* (14), 11652-11662.

8. Chen, S.; Wang, L.-W., Thermodynamic Oxidation and Reduction Potentials of Photocatalytic Semiconductors in Aqueous Solution. *Chemistry of Materials* **2012**, *24* (18), 3659-3666.
9. Gao, Y.; Zhang, S.; Bu, X.; Tian, Y., Surface defect engineering via acid treatment improving photoelectrocatalysis of  $\beta$ - $\text{In}_2\text{S}_3$  nanoplates for water splitting. *Catalysis Today* **2019**, *327*, 271-278.
10. Tian, W.; Chen, C.; Meng, L.; Xu, W.; Cao, F.; Li, L., PVP Treatment Induced Gradient Oxygen Doping in  $\text{In}_2\text{S}_3$  Nanosheet to Boost Solar Water Oxidation of  $\text{WO}_3$  Nanoarray Photoanode. *Advanced Energy Materials* **2020**, *10* (18).
11. Chen, D.; Liu, Z., Efficient Indium Sulfide Photoelectrode with Crystal Phase and Morphology Control for High-Performance Photoelectrochemical Water Splitting. *ACS Sustainable Chemistry & Engineering* **2018**, *6* (9), 12328-12336.
12. Hsieh, P. Y.; Chiu, Y. H.; Lai, T. H.; Fang, M. J.; Wang, Y. T.; Hsu, Y. J.,  $\text{TiO}_2$  Nanowire-Supported Sulfide Hybrid Photocatalysts for Durable Solar Hydrogen Production. *ACS Appl Mater Interfaces* **2019**, *11* (3), 3006-3015.
13. Wang, L.; Xia, L.; Wu, Y.; Tian, Y., Zr-Doped  $\beta$ - $\text{In}_2\text{S}_3$  Ultrathin Nanoflakes as Photoanodes: Enhanced Visible-Light-Driven

Photoelectrochemical Water Splitting. *ACS Sustainable Chemistry & Engineering* **2016**, 4 (5), 2606-2614.

## **Chapter 2**

### **All-Solution-Processed WO<sub>3</sub>/BiVO<sub>4</sub> Core–Shell Nanorod Arrays for Highly Stable Photoanodes**

## 2.1. Introduction

Sustainable energy production technology has been widely researched because of global environmental issues and increasing demands of energy.<sup>1-</sup>

<sup>2</sup> The new energy should be at a scale and a cost that can compete with fossil fuels. In this regard, the photoelectrochemical (PEC) cell, which converts solar energy directly to chemical energy, is one of the most promising candidates for clean and efficient energy technology.<sup>3-5</sup> There have been numerous reports on oxide semiconductor materials such as  $\text{WO}_3$ ,<sup>6-8</sup>  $\text{BiVO}_4$ ,<sup>9-</sup>  
<sup>11</sup>  $\alpha\text{-Fe}_2\text{O}_3$ ,<sup>12-13</sup>  $\text{TiO}_2$ ,<sup>14</sup> and  $\text{SnO}_2$ <sup>15</sup> for photoelectrodes over the past decades. Among the various oxide semiconductors,  $\text{WO}_3$  has attracted great interest for photoanodes. Owing to its moderate band gap of 2.5-2.7 eV,  $\text{WO}_3$  can absorb wide range of wavelengths including visible light.<sup>6</sup> It also has appropriate band-edge position for spontaneous PEC reaction and good electron transport properties due to the moderate hole diffusion length.<sup>8, 16</sup> Nonetheless,  $\text{WO}_3$  alone as a photoanode has limitations of poor charge separation, fast recombination of photo-generated electron-hole pairs, and less utilization of solar irradiation.<sup>17-19</sup> This limitation can be overcome by controlling nanostructure,<sup>20-21</sup> forming type II heterojunctions with other materials,<sup>22-25</sup> and employing co-catalysts on the surface.<sup>26</sup>

To improve PEC properties of photoelectrodes, much efforts to control nanostructures has been made. Nanostructures such as nanoplates, nanorods,

nanotubes, and nanowires with large surface area rather than bulk particles are favorable to enhance the incident-photon-to-current efficiency of photoelectrodes.<sup>16,27</sup> Especially, 1-dimensional nanorods of high crystallinity are suitable for photoanodes owing to short distances for holes to diffuse to the solid/liquid interface as well as large surface area that can absorb incident light sufficiently.<sup>6, 28</sup> There are various methods to produce oxide nanostructures such as sol-gel,<sup>29-30</sup> electrodeposition,<sup>31-32</sup> hydrothermal,<sup>16, 33-34</sup> anodization,<sup>13</sup> pulsed laser deposition,<sup>10</sup> chemical vapor deposition,<sup>21</sup> physical vapor deposition,<sup>35</sup> and so on. The methods that use vacuum equipment can control the morphology of nanostructures with high reproducibility. However, it should be noted that our goal is to produce energy that is sustainable and the production process should be environment-friendly and low-cost. Since the operation of vacuum equipment is energy-intensive, it does not meet our criteria. On the other hand, solution processes are rather eco-friendly and low-cost technology because most of the solution processes does not need to be performed in extreme conditions such as low pressure and high temperature.

Recently, constructing type II heterojunctions has been extensively studied to further enhance PEC properties of photoanodes. In particular,  $\text{WO}_3/\text{BiVO}_4$  heterojunction is one of the most attractive combinations for a photoanode to improve charge separation and optical absorption owing to their appropriate

band-edge positions and the smaller band gap energy of BiVO<sub>4</sub> than WO<sub>3</sub>. According to the previously reported papers, WO<sub>3</sub>/BiVO<sub>4</sub> heterojunction photoanodes showed much improved photoactivity compared to the pristine WO<sub>3</sub> photoanodes.<sup>25, 31</sup> However, the PEC properties of photoanode prepared with BiVO<sub>4</sub> are usually lower when the light flashes on the front side than back side because of the short diffusion length of BiVO<sub>4</sub>.<sup>26, 31, 36-38</sup> In addition, solution processed WO<sub>3</sub>/BiVO<sub>4</sub> photoanodes often show poor long-term stability.<sup>22, 36-37</sup> These facts become serious drawbacks when it is applied in industry where a tandem cell should be formed and operate for a long time.<sup>9, 39</sup>

Here, we report all-solution processed WO<sub>3</sub>/BiVO<sub>4</sub> hetero-nanostructure photoanodes with high performance. To reduce process steps for a facile fabrication, the hydrothermal synthesis was performed without seed layer on the substrate. BiVO<sub>4</sub> was conformally coated by pulsed electrodeposition on hydrothermally synthesized WO<sub>3</sub> nanorods. After annealing, we could achieve highly photoactive monoclinic WO<sub>3</sub> and monoclinic BiVO<sub>4</sub> resulting in high photocurrent density. The optimum WO<sub>3</sub>/BiVO<sub>4</sub> photoanode showed the photocurrent density of 4.15 mA/cm<sup>2</sup> at 1.23 V (vs. RHE) which is more than double that of pristine WO<sub>3</sub> nanorods. Also, the long-term stability was far improved by forming core-shell WO<sub>3</sub>/BiVO<sub>4</sub> structure. Despite of the short diffusion length of BiVO<sub>4</sub>, the PEC properties of WO<sub>3</sub>/BiVO<sub>4</sub>

heterojunction photoanode in this work are better with front illumination. We believe that our study could provide an important step to realize the sustainable hydrogen fuel community with photoelectrodes.

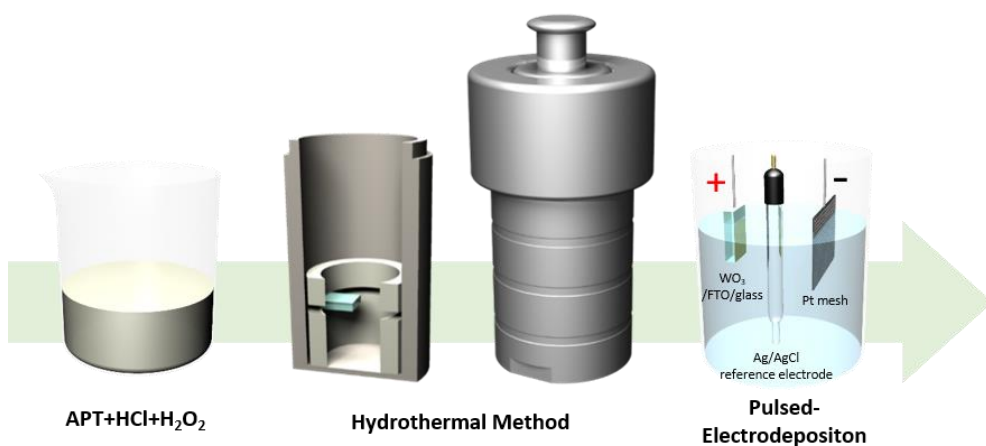


**Figure 2.1** Schematic illustration of  $\text{WO}_3/\text{BiVO}_4$  nanostructured photoanode fabrication.

## 2.2. Experimental Details

### 2.2.1. Synthesis of the WO<sub>3</sub> Nanorod Array

The one-dimensional WO<sub>3</sub> nanorod array was synthesized via a hydrothermal method with reference of a previous report.<sup>6</sup> The precursor solution was prepared by adding 0.3026 g of ammonium paratungstate powder ((NH<sub>4</sub>)<sub>10</sub>H<sub>2</sub>(W<sub>2</sub>O<sub>7</sub>)<sub>6</sub>, Aldrich) and 0.242 ml of concentrated hydrochloric acid (HCl, 35 %, DAEJUNG) in 23 ml of de-ionized water and stirring for 4 hours. Then 0.484 ml of hydrogen peroxide (H<sub>2</sub>O<sub>2</sub>, 30 %, DAEJUNG) was added to the yellowish-white opaque solution and stirred for at least 1 hour to get stable and transparent solution. The fluorine-doped SnO<sub>2</sub> (FTO) glass substrate, which was washed separately in acetone, ethanol, and de-ionized water and dried, was placed in a Teflon-lined stainless autoclave with the conductive side facing perfectly down by putting it between Teflon rings. The as-prepared solution was transferred into the autoclave and perfectly sealed. The synthesis was conducted at 120-180 °C in an oven for 4 hours and cooled down naturally to room temperature. After the reaction, the substrate was taken out, rinsed with DI water, and carefully dried. Then annealing was carried out at 500 °C for 2 h.

### **2.2.2. Preparation of WO<sub>3</sub>/BiVO<sub>4</sub> Heterojunction Photoanodes**

BiVO<sub>4</sub> was deposited on WO<sub>3</sub> nanorods by pulsed electrodeposition according to our previous report.<sup>31</sup> First, bismuth nitrate pentahydrate (BiN<sub>3</sub>O<sub>9</sub>, 98 %, JUN) and vanadium oxide sulfate hydrate (VOSO<sub>4</sub>, 99.99 %, Aldrich) were dissolved in de-ionized water adjusting pH to be less than 0.5 with nitric acid (HNO<sub>3</sub>, 67 %, JUN). By adding 2 M sodium acetate (CH<sub>3</sub>COONa, Aldrich) and a few drops of concentrated HNO<sub>3</sub>, the pH of the solution was adjusted to 4.7, because vanadium (IV) precipitates can be formed at pH > 5. Pulsed electrodeposition was conducted at 80 °C in a three-electrode system, in which hydrothermally grown WO<sub>3</sub> nanorods array on FTO glass, Ag/AgCl, a Pt mesh were used as working, reference, and counter electrode, respectively. The potential was cycled between 1.95 V and 0 V. After the deposition, the sample was rinsed with de-ionized water and annealed at 500 °C for 6 h.

### **2.2.3. Material Characterization**

The morphology of pristine WO<sub>3</sub> nanorods and WO<sub>3</sub>/BiVO<sub>4</sub> heterojunction nanostructure was investigated by a field-emission scanning electron microscope (FESEM, ZEISS, MERLIN Compact). Transmission electron microscope (TEM, JEOL JEM 3000F) analysis was conducted to characterize core-shell nanostructure of WO<sub>3</sub>/BiVO<sub>4</sub> heterojunctions. The crystalline

phase of pristine WO<sub>3</sub> and WO<sub>3</sub>/BiVO<sub>4</sub> nanorods was determined by X-ray diffractometer (XRD, BRUKER, D8-Advance).

#### **2.2.4. PEC Measurements**

PEC measurements were conducted using a potentiostat (Ivium Technologies, Nstat) in a three-electrode system composed of the prepared sample as working electrode, Ag/AgCl/saturated KCl as a reference electrode, and a Pt wire as a counter electrode. The potentials vs Ag/AgCl were converted to the RHE using Nernst relation:  $E_{\text{RHE}} = E^0_{\text{Ag/AgCl}} + E_{\text{Ag/AgCl}} + 0.059 * \text{pH}$  where  $E_{\text{RHE}}$  is the converted potential vs. RHE, the reference potential of Ag/AgCl,  $E^0_{\text{Ag/AgCl}}$  is 0.198 V, and  $E_{\text{Ag/AgCl}}$  is the measured potentials against RHE and Ag/AgCl. For the electrolyte, 0.5 M potassium phosphate buffer (pH 7) containing 1 M sodium sulfite (Na<sub>2</sub>SO<sub>3</sub>, WAKO) as a hole scavenger was used. Linear sweep voltammetry (LSV) measurements were performed at a scan rate of 10 mV/s under AM 1.5G simulated solar light illumination which was calibrated to 1 sun (100 mW/cm<sup>2</sup>) using reference cell. Electrochemical impedance spectroscopy (EIS) spectra were collected in the same three-electrode system sweeping 350 kHz to 1 Hz with an AC amplitude of 10 mV and fitted using the ZsimpWin software. The incident photon-to-current efficiency (IPCE) was measured with an irradiation source and monochromator (MonoRa150). The oxygen evolution was measured by gas

chromatography measurement system (Agilent GC 7890B) with a thermal conductivity detector and a micropacked column (ShinCarbon ST 100/120) in a gas-tight two-compartment electrochemical cell with a piece of Nafion 117 anion exchange membrane as a separator in 0.5 M phosphate buffer (pH 7) solution under AM 1.5G simulated solar light illumination.<sup>40-42</sup>

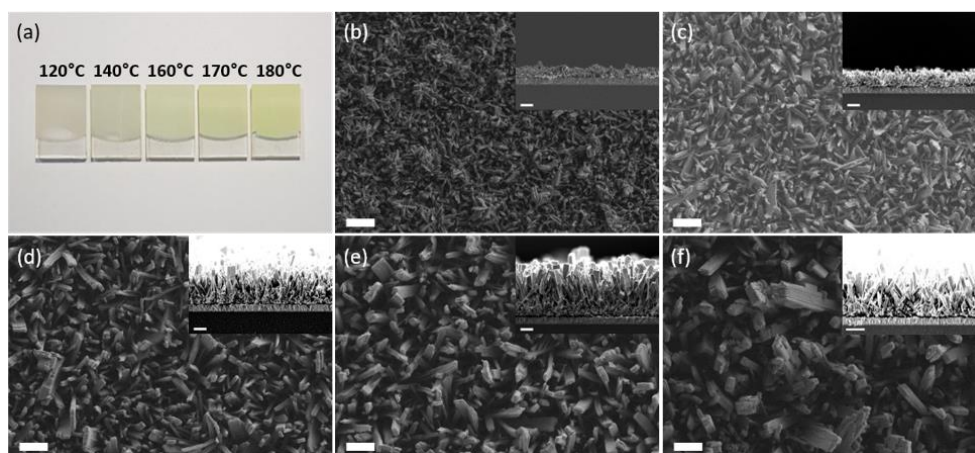
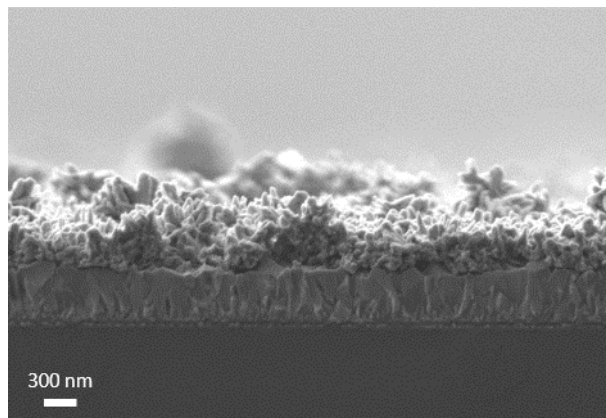


**Figure 2.2** (a) Photographic images of  $\text{WO}_3$  anodes synthesized at different temperatures. SEM images of  $\text{WO}_3$  nanorods synthesized at (b) 120, (c) 140, (d) 160, (e) 170, and (f) 180 °C for 4 h. The insets are the cross-sectional view of nanorods on FTO.

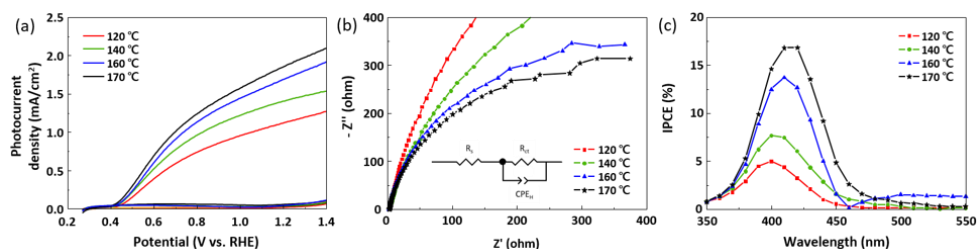
### 2.3. Results and discussion

Figure 2.1 shows an illustration of the overall sample preparation process of  $\text{WO}_3/\text{BiVO}_4$  photoanodes on FTO glass.  $\text{WO}_3$  nanorods were formed by hydrothermal method on FTO substrate in stabilized tungstic acid solution which was prepared by mixing ammonium paratungstate solution, concentrated HCl, and  $\text{H}_2\text{O}_2$ . The FTO substrate was put between Teflon rings with the conductive side facing down to avoid the interruption to growth by impurities. After the sample is naturally cooled down and annealed for adhesion and phase transition, pulsed electrodeposition was conducted to attach  $\text{BiVO}_4$  on  $\text{WO}_3$  nanorods. First of all, we controlled various conditions to find the optimum morphology of  $\text{WO}_3$  for photoanodes. Figure 2.2a shows a photograph of  $\text{WO}_3$  nanorods synthesized at different temperature. The nanorods covered the entire surface of FTO substrates where the solution could reach. All samples exhibited uniform yellowish color which was deepened with increasing reaction temperature, indicating the size of nanorods was enlarged. The SEM images (Figure 2.2b-f) confirmed that vertically grown  $\text{WO}_3$  nanorods covered the substrate uniformly without a seed layer and the average diameter and thickness of rods were increased as the temperature increases. The  $\text{WO}_3$  nanorods synthesized at 170 °C have diameter of 150-300 nm and thickness of 4  $\mu\text{m}$ . The diameter of rods was fairly even at reaction temperature of 120 °C to 170 °C, but there were some

bulky rods with diameter of 600-700 nm which can decline PEC performance by shading a light at 180 °C. Since the hydrothermal reaction was conducted without an assistance of a seed layer, the nuclei, which were further grew as small rods without certain directionality, were formed on the surface at the beginning of reaction without any empty surface regions (Figure 2.3). Then, only the rods formed perpendicular to the substrate further grew as nanorods.



**Figure 2.3** Cross-section SEM images of hydrothermally synthesized  $\text{WO}_3$  at 170 °C for 30 minutes



**Figure 2.4** (a) Linear sweep voltammograms tested at a scan rate of 10 mV/s under AM 1.5 G solar light, (b) electrochemical impedance spectra measured at 0.6 V vs. Ag/AgCl, and (c) incident photon-to-current efficiency data at 0.6 V vs. Ag/AgCl for pristine WO<sub>3</sub> nanorods synthesized at different temperature. Inset shows equivalent circuits for all WO<sub>3</sub> nanorods. All measurements were carried in 0.5 M phosphate buffer (pH 7) with 1 M Na<sub>2</sub>SO<sub>3</sub>.

**Table 2.1** Fitted series resistance ( $R_s$ ) and charge transfer resistance ( $R_{ct}$ ) across the electrolyte/anode interface of pristine WO<sub>3</sub> nanorods synthesized at different temperature.

Temperature (°C)	$R_s$ ( $\Omega \cdot \text{cm}^2$ )	$R_{ct}$ ( $\Omega \cdot \text{cm}^2$ )
120	2.53	2348
140	2.82	1494
160	2.95	710
170	3.30	620

The photoactivity of the photoanodes was analyzed by measuring the photocurrent density using a standard three-electrode cell immersed in 0.5 M potassium phosphate buffer (pH 7) containing 1 M Na<sub>2</sub>SO<sub>3</sub> at a scan rate of 10 mV/s under AM 1.5 G simulated solar light (Figure 2.4). Because sulfite oxidation is thermodynamically and kinetically favorable than water oxidation, sodium sulfite acts as a hole scavenger which enables direct comparison of the photocurrent density without considering water oxidation kinetics.<sup>43</sup> Figure 2.4a shows linear sweep voltammograms of WO<sub>3</sub> nanorods synthesized at different temperature. For all WO<sub>3</sub> nanorods except for the sample prepared at 120 °C, a noticeable photocurrent started at low bias of 0.4 V vs. RHE suggesting that a good charge separation was occurred under solar illumination. As the reaction temperature increased from 120 to 170 °C, the photocurrent density increased from 1.14 to 1.97 mA/cm<sup>2</sup> at 1.23 V vs. RHE. This is attributed to the increased active sites as the size of nanorods enlarged. On the other hand, the photocurrent density decreased to 1.58 mA/cm<sup>2</sup> at 1.23 V vs. RHE when the reaction temperature reached to 180 °C (Figure 2.5a). This result was already expected since the bulky rods between small nanorods shaded the light so that the small rods were unable to produce electron-hole pairs in light although the surface area was increased. Also, the photoactivity of WO<sub>3</sub> nanorods with different reaction time was measured.

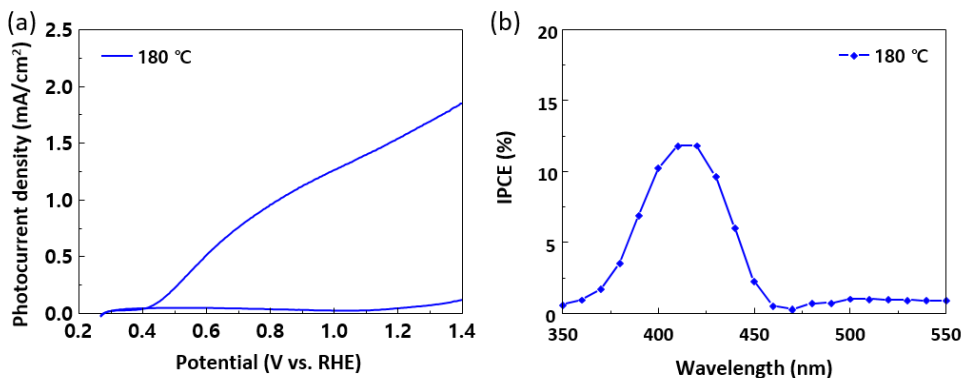


**Figure 2.5** (a) Linear sweep voltammogram and (b) incident photon-to-current efficiency data of pristine WO<sub>3</sub> anodes synthesized at 180 °C tested in 0.5 M phosphate buffer (pH 7) with 1 M Na<sub>2</sub>SO<sub>3</sub> at a scan rate of 10 mV/s under AM 1.5 G solar light.

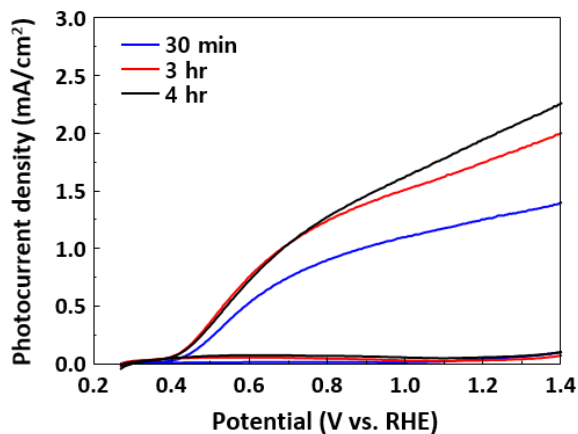


**Figure 2.6** Linear sweep voltammograms of pristine WO<sub>3</sub> anodes synthesized for different time tested in 0.5 M phosphate buffer (pH 7) with 1 M Na<sub>2</sub>SO<sub>3</sub> at a scan rate of 10 mV/s under AM 1.5 G solar light.

The photocurrent density was increased from 1.26 to 1.97 mA/cm<sup>2</sup> at 1.23 V vs. RHE as the reaction time increased from 30 minutes to 4 h (Figure 2.6). The nanorods array was peeled off when the synthesis lasted for more than 5 hours. Next, the concentration of tungsten precursor was controlled. Because the solubility of ammonium paratungstate is extremely low in aqueous solution, the maximum concentration was 0.06 M of tungsten but the nanorods array synthesized in this concentration of solution was easily peeled off during rinsing with DI water. The photocurrent density of WO<sub>3</sub> nanorods with 0.05 M of tungsten was the optimum as shown in Figure 2.7. The PEC performances of WO<sub>3</sub> photoanodes reported previously are shown in Table

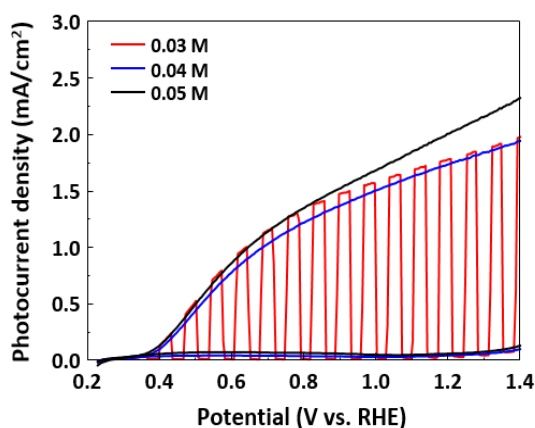


**Figure 2.7** Linear sweep voltammograms of pristine WO<sub>3</sub> anodes synthesized with the solution of different W concentration tested in 0.5 M phosphate buffer (pH 7) with 1 M Na<sub>2</sub>SO<sub>3</sub> at a scan rate of 10 mV/s under AM 1.5 G solar light.

2.2. It shows that the photocurrent density of our WO<sub>3</sub> photoanode is comparable to those of others.

**Table 2.2** PEC performance of the reported WO<sub>3</sub> photoanodes.

Ref.	Method	Morphology	Electrolyte	Photocurrent density (mA/cm <sup>2</sup> )	Year
6	Hydrothermal	Nanorods	0.5 M Na <sub>2</sub> SO <sub>4</sub>	2.26 (1.23 V vs. RHE)	2013
44	Hydrothermal	Nanorods	0.5 M Na <sub>2</sub> SO <sub>4</sub>	0.5 (1.23 V vs. RHE)	2014
20	Hydrothermal	Nanoplates	0.5 M Na <sub>2</sub> SO <sub>4</sub>	1.88 (1.3 V vs. Ag/AgCl)	2016
16	Hydrothermal	Nanoplates	0.5 M Na <sub>2</sub> SO <sub>4</sub>	1.0 (1.6 V vs. RHE)	2017
45	Sol-gel	Mesoporous film	1 M CH <sub>3</sub> SO <sub>3</sub> H	4.2 (1.23 V vs. RHE)	2018
46	Hydrothermal	Nanorods	0.5 M Na <sub>2</sub> SO <sub>4</sub> + 0.2 M Na <sub>2</sub> SO <sub>3</sub>	0.4 (1.23 V vs. RHE)	2018
47	Pulsed laser deposition	Thin film	0.5 M H <sub>2</sub> SO <sub>4</sub>	1.8 (1.23 V vs. RHE)	2019
48	Hydrothermal	Nanoplates	0.5 M Na <sub>2</sub> SO <sub>4</sub>	4.12 (1.6 V vs. Ag/AgCl)	2019
This work	Hydrothermal	Nanorods	0.5 M KPi (pH 7) + 1 M Na <sub>2</sub> SO <sub>3</sub>	1.97 (1.23 V vs. RHE)	

To investigate the dynamics of carrier transport and recombination of the pristine WO<sub>3</sub> photoanodes, electrical impedance spectroscopy (EIS) measurements were carried out in a frequency range of 350 KHz to 1 Hz with amplitude of 10 mV at 0.6 V vs Ag/AgCl. Figure 2.4b shows the Nyquist plots of WO<sub>3</sub> nanorods with different reaction temperature. The diameter of the semicircle in the Nyquist plot which equals charge transfer resistance across the electrolyte/anode interface was decreased as the current density increases indicating good charge transfer property contributes to the high photoactivity.<sup>32, 49-50</sup> The equivalent circuit model was constructed on the basis of the experimental data to confirm this results with the exact values where R<sub>s</sub> and R<sub>ct</sub> represent the series resistance and charge transfer resistance as illustrated in Figure 2.4b.<sup>51</sup> The fitted values of R<sub>ct</sub> were 2348, 1494, 710, and 620 Ω·cm<sup>2</sup> for a sample synthesized at 120, 140, 160, and 170 °C, respectively, as displayed in Table 2.1. Incident-photon-to-current conversion efficiency (IPCE) spectra was measured from 350 to 550 nm at 0.6 V vs Ag/AgCl to explore the photoactivity of the WO<sub>3</sub> nanorods as shown in Figure 2.4c. The values were calculated by the equation  $IPCE (\%) = (1240 * J_{photo}) / \lambda * P_{inc}$  where J<sub>photo</sub> is photocurrent density (mA/cm<sup>2</sup>), λ is the wavelength of incident light (nm), and P<sub>inc</sub> is the incident power density (mW/cm<sup>2</sup>). The maximum intensity of the optimum WO<sub>3</sub> nanorods

synthesized at 170 °C reached 16.8 % at 420 nm as shown in Figure 2.4c and Figure 2.5b.

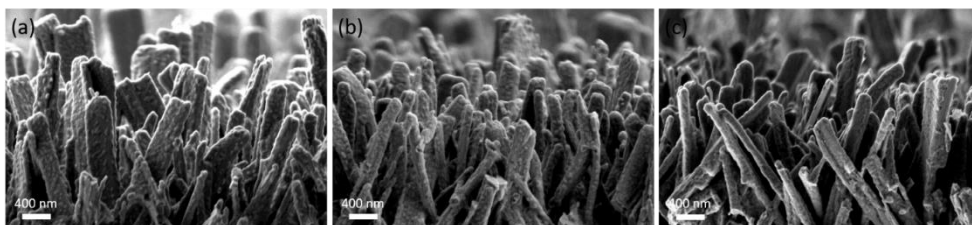


**Figure 2.8** Cross-section SEM images of  $\text{WO}_3/\text{BiVO}_4$  heterojunction nanostructures, in which  $\text{BiVO}_4$  were formed by (a) 3, (b) 6, and (c) 9 cycles of pulsed electrodeposition on optimum  $\text{WO}_3$  nanorods synthesized by hydrothermal method.

To enhance the PEC performance of  $\text{WO}_3$  photoanodes, pulsed electrodeposition of  $\text{BiVO}_4$  was conducted on hydrothermally synthesized  $\text{WO}_3$  nanorods to form  $\text{WO}_3/\text{BiVO}_4$  heterojunction anodes. Electrodeposition with pulsed voltage facilitates precursors to diffuse deep into the nanostructure during pulsed off time lowering the concentration gradient of ions in the solution near the surface of nanorods and then leading to the uniform coating.<sup>31</sup> The cross-sectional SEM images of  $\text{WO}_3/\text{BiVO}_4$  heterojunction nanostructures are presented in Figure 2.8.  $\text{BiVO}_4$  was conformally coated on the surface of  $\text{WO}_3$  nanorods without destroying the 1D nanostructure of  $\text{WO}_3$ . In the case of 3 and 6 cycles of pulsed

electrodeposition, distinct nanodots could be seen with the average diameter of 50 nm (Figure 2.8a and 2.8b, referenced as WO<sub>3</sub>/3-BVO and WO<sub>3</sub>/6-BVO, respectively). The density of BiVO<sub>4</sub> nanodots on the surface of the nanorods was increased when the number of coating cycles increases. Finally, BiVO<sub>4</sub> with more than 9 cycles of deposition (referenced as WO<sub>3</sub>/9-BVO) almost covered the entire surface of WO<sub>3</sub> nanorods and assembled to form a thin film resulting in a core-shell structure of WO<sub>3</sub>/BiVO<sub>4</sub> as shown in Figure 2.8c. The core-shell structure with extremely thin absorber layer has advantage of high separation efficiency because photo-generated electrons can move fast to the heterojunction interface.<sup>35</sup> Also, long core-shell nanorods have equal efficiency in all incident angle.<sup>35</sup>

To investigate the detailed morphology and the formation of WO<sub>3</sub>/BiVO<sub>4</sub> core-shell heteronanostructure, transmission electron microscope (TEM) analysis was carried out. Energy-dispersive X-ray spectroscopy (EDS) elemental maps corresponding to a single WO<sub>3</sub>/9-BVO nanorod (Figure 2.9a) are shown in Figure 2.9b-e. According to Figure 2.9c and 2.9d, BiVO<sub>4</sub> uniformly covered the WO<sub>3</sub> nanorod forming core-shell structure. The thickness of BiVO<sub>4</sub> on WO<sub>3</sub> was around 12 nm for WO<sub>3</sub>/9-BVO which is greatly shorter than the hole diffusion length of BiVO<sub>4</sub> (~80 nm) as shown in Figure 2.9f. WO<sub>3</sub> nanorods were grown with *d*-spacing of 0.37 nm and 0.38 nm, corresponding to the (110) and (002) planes of monoclinic WO<sub>3</sub> and the

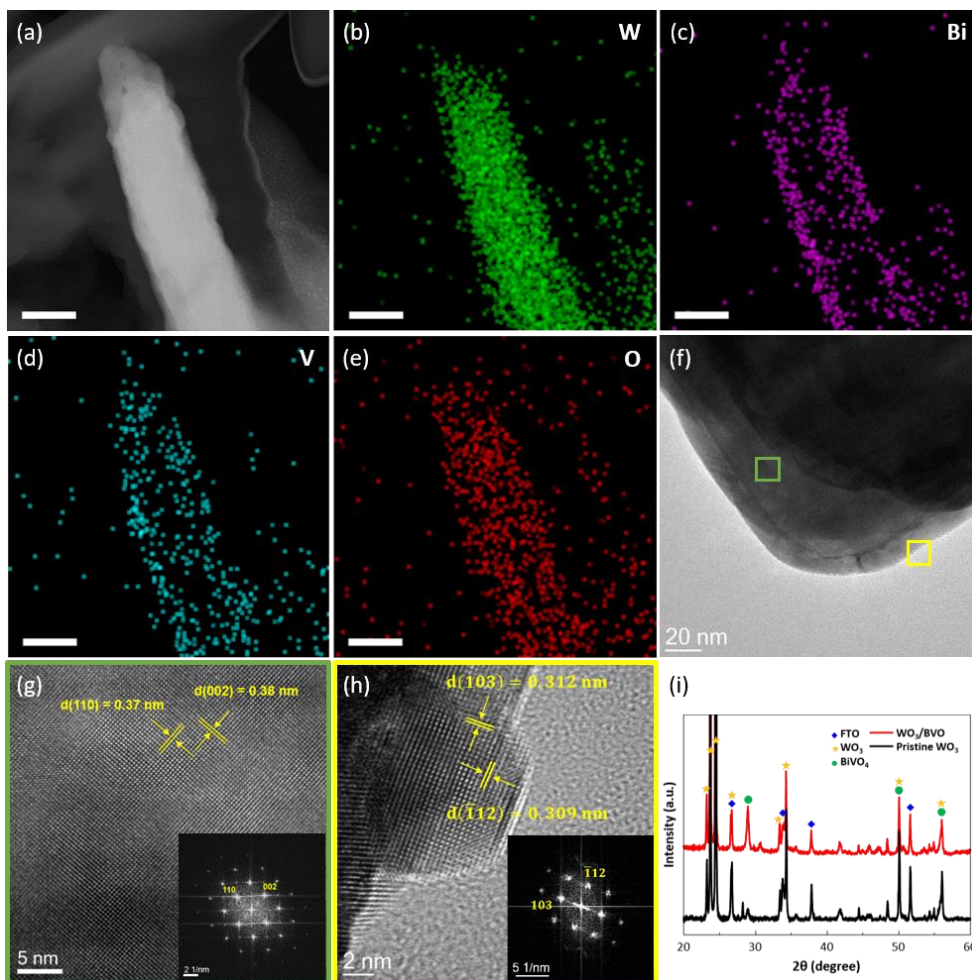


**Figure 2.9** (a) TEM image of a WO<sub>3</sub>/9-BVO nanorod and corresponding EDS element maps of (b) W, (c) Bi, (d) V, and (e) O respectively. The scale bar is 100 nm for (a-e). (f) TEM image of a WO<sub>3</sub>/9-BVO nanorod with uniform thickness of BiVO<sub>4</sub>. (g, h) High-resolution TEM and selected area diffraction pattern (inset) showing (g) crystalline plane of (110) and (002) of monoclinic WO<sub>3</sub> and (h) crystalline plane of (103) and (112) of monoclinic BiVO<sub>4</sub>. (i) X-ray diffraction patterns of pristine WO<sub>3</sub> and WO<sub>3</sub>/BVO photoanodes.

BiVO<sub>4</sub> layer were deposited with *d*-spacing of 0.312 nm and 0.309 nm, corresponding to the (103) and (112) of monoclinic BiVO<sub>4</sub> as shown in High-resolution TEM (HR-TEM) image and the selected area electron diffraction (SAED) pattern (Figure 2.9g, h). The HR-TEM image and the SAED pattern of BiVO<sub>4</sub> in Figure 2.9h were obtained after the BiVO<sub>4</sub> is destroyed during TEM analysis. Zhang et al.<sup>52</sup> reported about this phenomenon that monoclinic BiVO<sub>4</sub> layer transforms to monoclinic BiVO<sub>4</sub> quantum dots under high-energy electron beam within 5 seconds. The TEM image after the destruction is shown in Figure 2.10. The existence of WO<sub>3</sub> and BiVO<sub>4</sub> could be also seen in the X-ray diffraction (XRD) patterns. The peaks of monoclinic WO<sub>3</sub> (JCPDS: 43-1035) were clearly shown for the pristine WO<sub>3</sub> nanorods. Also, for the WO<sub>3</sub>/BiVO<sub>4</sub> heterostructures, the peaks were well-indexed to monoclinic WO<sub>3</sub> and monoclinic BiVO<sub>4</sub> (JCPDS: 14-0688) which are photoactive.

PEC measurements were conducted for the comparison of pristine WO<sub>3</sub> and WO<sub>3</sub>/BiVO<sub>4</sub> heterojunction photoanodes. Figure 2.11a shows chopped linear sweep voltammograms of photoanodes with different number of coating cycles. The photocurrent density was increased with increasing the number of coating cycles until 9 times, however, when the deposition was carried out over 9 cycles, the photocurrent density rather decreased sharply. Because the BiVO<sub>4</sub> covered the entire surface of the nanorods with 9 cycles of deposition,

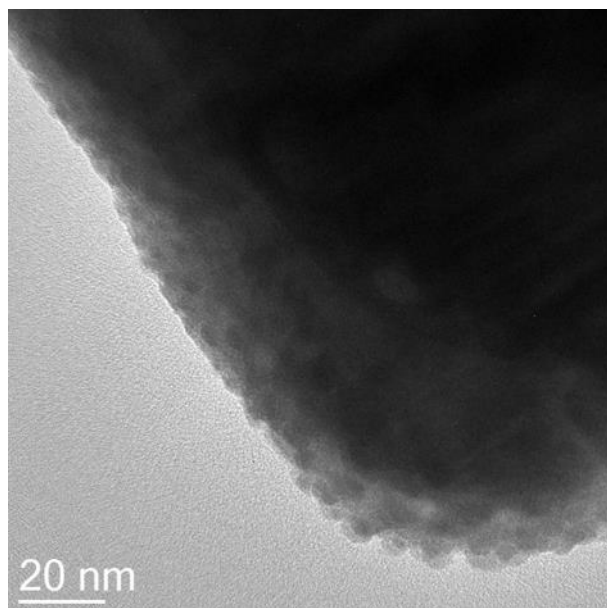


**Figure 2.10** TEM image of a  $\text{WO}_3/9\text{-BVO}$  nanorod to show the formation of  $\text{BiVO}_4$  nanodots under high-energy electron beam.

the thickness of  $\text{BiVO}_4$  layer would increase as the number of deposition cycles increases and the recombination of electron-hole pairs would be increased due to the short diffusion length of  $\text{BiVO}_4$  resulting the reduction of photocurrent density. The highest photocurrent density which was obtained with  $\text{WO}_3/9\text{-BVO}$  was  $4.15 \text{ mA/cm}^2$  at  $1.23 \text{ V vs. RHE}$  in  $0.5 \text{ M}$  phosphate buffer ( $\text{pH } 7$ ) with  $1 \text{ M Na}_2\text{SO}_3$  under front illumination which is double that of pristine  $\text{WO}_3$ . EIS spectra were collected in a frequency range of  $350 \text{ KHz}$  to  $1 \text{ Hz}$  with amplitude of  $10 \text{ mV}$  at  $1.23 \text{ V vs. RHE}$ . The smaller diameter of arc for the  $\text{WO}_3/\text{BiVO}_4$  nanostructure than pristine  $\text{WO}_3$  in the Nyquist plot

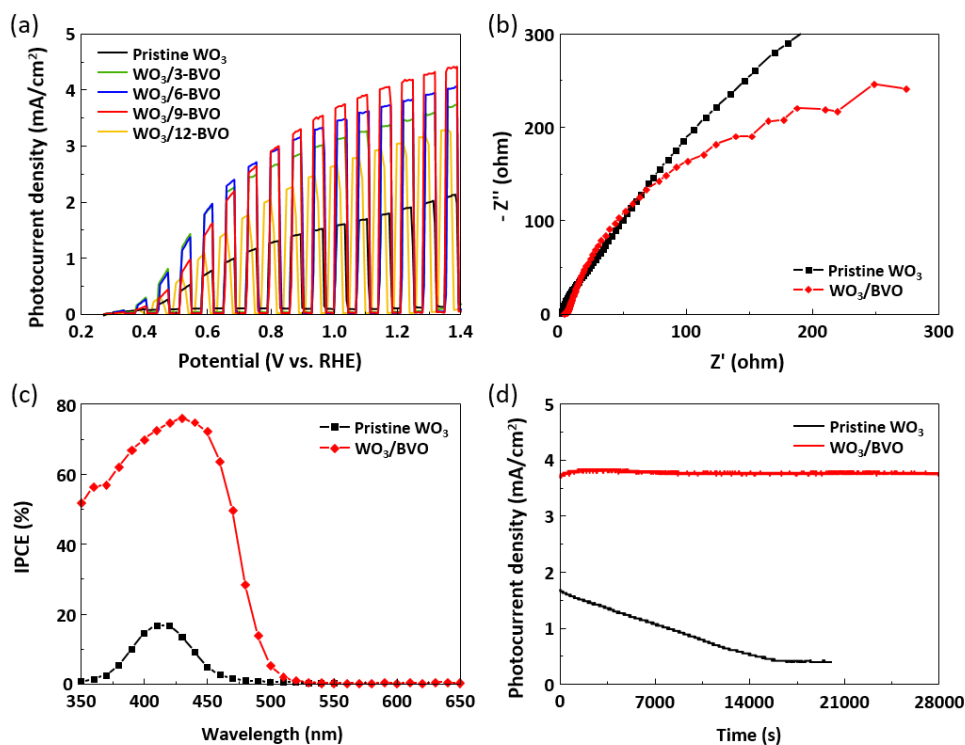


**Figure 2.11** (a) Chopped linear sweep voltammograms with different numbers of cycles for BiVO<sub>4</sub> deposition tested in 0.5 M phosphate buffer (pH 7) with 1 M Na<sub>2</sub>SO<sub>3</sub> at a scan rate of 10 mV/s under front illumination, (b) electrochemical impedance spectra, (c) incident photon-to-current efficiency data, and (d) stability test data measured at 1.23 V vs. RHE for pristine WO<sub>3</sub> and WO<sub>3</sub>/BVO photoanodes.

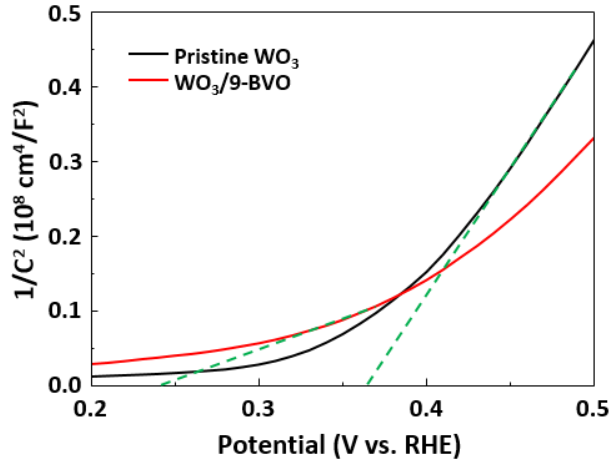


**Figure 2.12** Mott-Schottky plots for optimized pristine  $\text{WO}_3$  and  $\text{WO}_3/9\text{-BVO}$  anodes measured in 0.5 M phosphate buffer (pH 7) with 1 M  $\text{Na}_2\text{SO}_3$ .

### Mott-Schottky Relation

$$\frac{1}{C^2} = \left( \frac{2}{e\epsilon_r\epsilon_0 A^2 N_d} \right) \left( V - V_{FB} - \frac{k_B T}{e} \right) \quad (2.1)$$

C [F]: space charge layers capacitance

e: electron charge ( $1.602 \times 10^{-19}$  C)

$\epsilon_r$ : dielectric constant of semiconductor

$\epsilon_0$ : permittivity of vacuum ( $8.854 \times 10^{-14}$  F m<sup>-1</sup>)

A [cm<sup>2</sup>]: active area of the photoanode

$N_d$  [cm<sup>-3</sup>]: donor density

V: applied potential (vs. RHE)

$V_{FB}$ : flat band potential (vs. RHE)

$k_B$ : Boltzmann constant ( $1.381 \times 10^{-23}$  J K<sup>-1</sup>)

T [K]: temperature

(Figure 2.11b) indicates charge transfer resistance of the heterojunction photoanode is lower than pristine WO<sub>3</sub> nanorods.<sup>32, 49-50</sup> The IPCE spectra of WO<sub>3</sub>/BiVO<sub>4</sub> presented in Figure 2.11c showed that the intensity of the WO<sub>3</sub>/BiVO<sub>4</sub> significantly enhanced to 75.9 % at 430 nm which was 4.5 times higher than pristine WO<sub>3</sub>.

To estimate the flat band potential and carrier density of each photoanodes, Mott-Schottky analysis was carried out for pristine WO<sub>3</sub> and WO<sub>3</sub>/9-BVO by EIS measurement at 1 kHz in dark. According to the Mott-Schottky relation (Figure 2.12), the intercept of the x-axis and the slope for the tangent of the linear region each represent flat band potential and the charge carrier density in a capacitance-potential plot ( $1/C^2$  vs. V).<sup>41</sup> The flat band potential was shifted to negative by 112 mV after forming heterojunction, indicating that lower external bias is required for WO<sub>3</sub>/9-BVO to drive PEC reaction compared to the single anode which corresponds to the tendency of measured

**Table 2.3** Flat band potential and donor density for WO<sub>3</sub> and WO<sub>3</sub>/9-BVO anodes.

<b>Samples</b>	<b>Flat band potential (V vs. RHE)</b>	<b>Donor density (cm<sup>-3</sup>)</b>
WO <sub>3</sub>	0.365	8.3 x 10 <sup>21</sup>
WO <sub>3</sub> /9-BVO	0.243	2.5 x 10 <sup>22</sup>

on-set potential in LSV. To obtain the charge carrier density, the real active area of the photoanodes should be included in the calculation. However, it is hard to confine the exact surface area of the nanostructure materials. In this paper, we assumed that the ratio of the planar area to the real active area for each anode is nearly equal because the heterojunction has core-shell structure. As a result, the donor density of  $\text{WO}_3/9\text{-BVO}$  was higher than that of pristine  $\text{WO}_3$  as shown in Table 2.3.

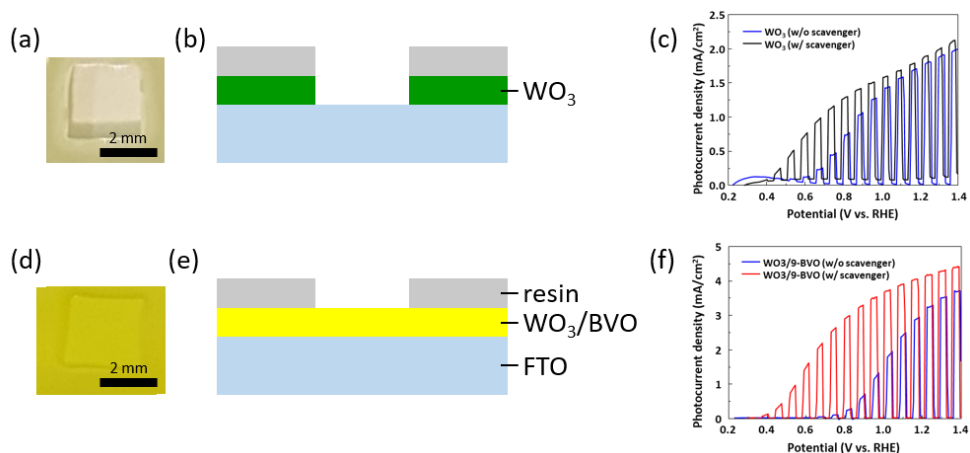


**Figure 2.13** (a, d) Photographic top-view images and (b, e) Schematic illustrations of cross-view of samples after stability test. Linear sweep voltammogram (LSV) of (c) optimized pristine  $\text{WO}_3$  and (f)  $\text{WO}_3/9\text{-BVO}$  anodes at a scan rate of 10 mV/s under AM 1.5 G solar light with and without using hole scavenger.

Furthermore, the stability test of photoanodes was conducted to see the possibility of commercial use. The photocurrent density at 1.23 V vs. RHE was recorded as a function of time. In the case of pristine  $\text{WO}_3$ , the photocurrent density started to decrease from the beginning of the test as shown in Figure 2.11d. After 4 hours of measurement, the  $\text{WO}_3$  nanorods array was perfectly peeled off as shown in Figure 2.13a and b. Meanwhile, the photocurrent density of  $\text{WO}_3/9\text{-BVO}$  was maintained even after 8 hours and the film was attached well on the substrate (Figure 2.13d and e).  $\text{WO}_3$  is well known to be thermodynamically stable.<sup>6, 53</sup> However,  $\text{WO}_3$  loses its photoactivity when the anodic reaction is continued for a long time due to the peroxy species produced on the surface even in acidic condition.<sup>53</sup> Moreover, the formation of peroxy species becomes easier in neutral and alkaline solution. Also, due to the absence of a seed layer during the synthesis, the adhesion of  $\text{WO}_3$  nanorods array was relatively weak. When  $\text{BiVO}_4$  was coated on the  $\text{WO}_3$  nanorods,  $\text{BiVO}_4$  covered entire surface of the anode forming core-shell structure. Therefore, it can be concluded that  $\text{BiVO}_4$  thin layer behaved as a passivation layer. In fact,  $\text{BiVO}_4$  has been well known to be photoelectrochemically unstable because of slow kinetics of oxygen evolution reaction. Also, the chemical stability of  $\text{BiVO}_4$  depends on the quality of the electrodes.<sup>54</sup> Owing to the high crystallinity of  $\text{BiVO}_4$  and good adhesion at the  $\text{BiVO}_4/\text{WO}_3$  interface of the photoanode produced by

electrodeposition, only the photostability should be controlled in this work. To avoid degradation of  $\text{BiVO}_4$  by photochemical reaction, hole scavenger,<sup>31</sup> co-catalyst,<sup>55</sup> passivation layer,<sup>22</sup> or back illumination<sup>36, 56</sup> was used in previously reported papers. The hole scavenger such as  $\text{Na}_2\text{SO}_3$  and  $\text{H}_2\text{O}_2$  can be used in the electrolyte leading fast charge injection on the surface of  $\text{BiVO}_4$ , enabling a long-term use.<sup>41</sup> However, the reaction with  $\text{Na}_2\text{SO}_3$  is not a pure water oxidation. Therefore, further works using co-catalysts should be progressed.

The photo-oxidation of water was measured for  $\text{WO}_3$  and  $\text{WO}_3/9\text{-BVO}$ . The measurement was performed in 0.5 M phosphate buffer solution (pH 7) without any hole scavenger. The photocurrent of  $\text{WO}_3/9\text{-BVO}$  anode for water oxidation was considerably lower than that for sulfite oxidation as shown in Figure 2.14a. Since the holes that were photo-generated and transported to the surface cannot be consumed fast at the surface of  $\text{BiVO}_4$  as mentioned above, they were accumulated and then recombined shortly. The oxygen evolution and the stability of  $\text{WO}_3/9\text{-BVO}$  were measured in 0.5 M phosphate buffer (pH 7) at 1.23 V vs RHE for 5400 s as shown in Figure 2.15 which shows nearly 100 % faradaic efficiency. The surface area was 0.6773  $\text{cm}^2$  and the photograph of the sample after the test is shown in Figure 2.15c. A decrease in the photocurrent was occurred during the stability test (Figure 2.15b) due to the slow elimination of hole on the surface and phosphate buffer

that etches BiVO<sub>4</sub>.<sup>57-58</sup> The photocurrent density starts at low level compared to the data in Figure 2.14a because the degradation of BiVO<sub>4</sub> by phosphate buffer has been proceeded during the nitrogen purging of several hours before the test even in dark condition.

To further investigate charge transfer and transport properties of the anodes, the charge transfer efficiency ( $\eta_{\text{trans}}$ ) and the charge separation efficiency ( $\eta_{\text{sep}}$ ) were estimated independently by following the equation:<sup>59-60</sup>

$$J_{\text{H}_2\text{O}} = J_{\text{max}} \eta_{\text{abs}} \eta_{\text{trans}} \eta_{\text{sep}} \quad (2.2)$$

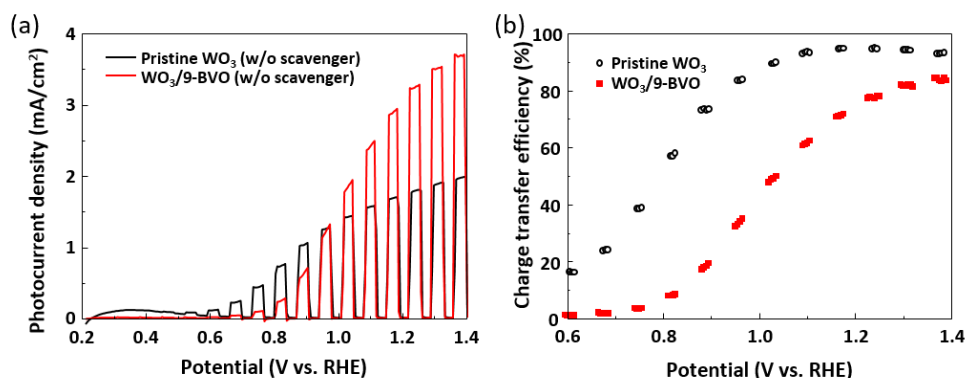


**Figure 2.14** (a) Linear sweep voltammogram (LSV) of optimized pristine WO<sub>3</sub> and WO<sub>3</sub>/9-BVO anodes tested in 0.5 M phosphate buffer (pH 7) at a scan rate of 10 mV/s under AM 1.5 G solar light and (b) charge transfer efficiency that was calculated by LSV data with and without using hole scavenger.

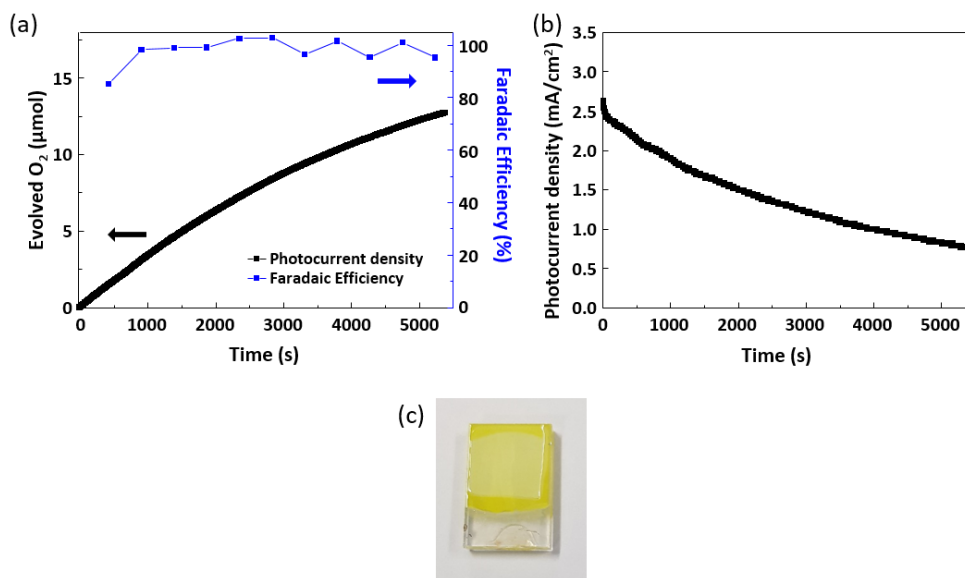


**Figure 2.15** (a) Oxygen evolution curve and corresponding faradaic efficiency, (b) stability test data for WO<sub>3</sub>/9-BVO anode. All the measurement was carried out in 0.5 M phosphate buffer (pH 7) at 1.23 V vs. RHE under AM 1.5 G solar light. (c) The photograph of the sample that used in O<sub>2</sub> evolution test.

where  $J_{\text{H}_2\text{O}}$  is the measured photocurrent density for water oxidation,  $J_{\text{max}}$  is the theoretical maximum photocurrent, and  $\eta_{\text{abs}}$  is the light absorption efficiency. Assuming that the charge transfer efficiency is 100 % in the Na<sub>2</sub>SO<sub>3</sub> solution, we can calculate the charge transfer efficiency at semiconductor/electrolyte interface by dividing the photocurrent density for water oxidation by that for sulfite oxidation ( $\eta_{\text{trans}} = J_{\text{H}_2\text{O}}/J_{\text{Na}_2\text{SO}_3}$ ). The charge transfer efficiency for pristine WO<sub>3</sub> was determined as 94 % which is higher

than 78 % for WO<sub>3</sub>/9-BVO at 1.23 V vs. RHE (Figure 2.14b). The charge transfer efficiency can be enhanced by using co-catalysts on the surface of anodes such as Co-Pi<sup>55</sup> and FeCoO<sub>x</sub><sup>61</sup> as previously reported. To calculate the charge separation efficiency, the absorption current density ( $J_{\text{abs}} = J_{\text{max}} \eta_{\text{abs}}$ ) for each sample was obtained by UV-vis transmission and reflectance spectroscopy first. Figure 2.16 shows the absorptance spectra of WO<sub>3</sub> and WO<sub>3</sub>/9-BVO. The absorption edge of the heterojunction anode was observed around 510 nm which corresponds to the band gap of BiVO<sub>4</sub>.  $J_{\text{abs}}$  for pristine WO<sub>3</sub> and WO<sub>3</sub>/9-BVO were derived to be 3.0 and 6.0 mA/cm<sup>2</sup>, respectively. The charge separation efficiency can be obtained by dividing  $J_{\text{Na}_2\text{SO}_3}$  by  $J_{\text{abs}}$  and the values were 62 and 70 % at 1.23 V vs. RHE for WO<sub>3</sub> and WO<sub>3</sub>/9-BVO, respectively. The calculated charge transfer and separation efficiency of the heterojunction anode are in good agreement with the values from the previously reported paper.<sup>17</sup> To sum up, the WO<sub>3</sub>/BiVO<sub>4</sub> heterojunction photoanode exhibited higher photocurrent density than optimum pristine WO<sub>3</sub> nanorods due to the ability to absorb wider range of light, good charge transport property, and low recombination rate.

The another point we should give attention is that all pec measurement was carried out under front illumination. Practical applications require high front-illumination photocurrent.<sup>9</sup> Unfortunately, the photoanodes containing BiVO<sub>4</sub> have higher photoactivity under back illumination rather than front

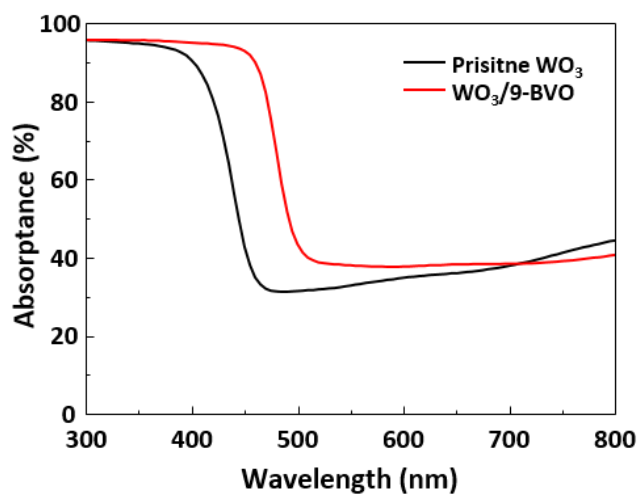


**Figure 2.16** Absorbance spectra of optimized pristine  $\text{WO}_3$  and  $\text{WO}_3/9\text{-BVO}$  anodes.

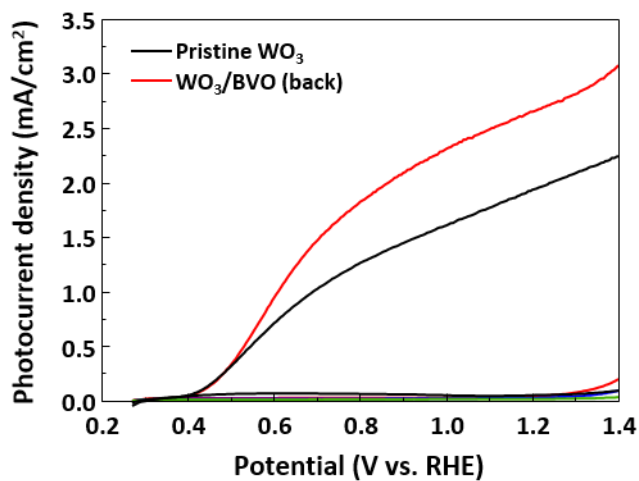


**Figure 2.17** Linear sweep voltammograms of  $\text{WO}_3/\text{BVO}$  anodes tested in 0.5 M phosphate buffer (pH 7) with 1 M  $\text{Na}_2\text{SO}_3$  at a scan rate of 10 mV/s under back illumination.

illumination in many cases.<sup>26, 31, 36-38</sup> Due to its short diffusion length of 80 nm, recombination readily occurs right after the electron-hole pairs are produced.<sup>31</sup> This can be overcome by downscaling BiVO<sub>4</sub> layer or doping.<sup>26, 38</sup> While back illumination is still superior even when the thickness of BiVO<sub>4</sub> layer is shorter than the diffusion length in some cases,<sup>31</sup> the WO<sub>3</sub>/BiVO<sub>4</sub> heterojunction photoanodes produced in our study have higher photocurrent density under front illumination as shown in Figure 2.17. This is attributed to the nanostructures of the photoanodes. The schematic illustrations of WO<sub>3</sub> and WO<sub>3</sub>/BiVO<sub>4</sub> photoanodes are depicted in Figure 2.18. Figure 2.18a shows the WO<sub>3</sub> nuclei that filled the entire substrate without certain directionality at the first stage of hydrothermal synthesis as mentioned above. Then the nuclei grown in the perpendicular direction to the substrate further grew as nanorods as shown in Figure 2.18b. As the pulsed electrodeposition progressed, BiVO<sub>4</sub> gradually covered the surface of WO<sub>3</sub> nanorods (Figure 2.18c). Finally, after 9 cycles of deposition, entire surface was covered constructing core-shell structure (Figure 2.18d). Due to the WO<sub>3</sub> nucleation process, density of the nanostructure near the substrate is too high for electrolyte to reach to the bottom of the sample for PEC measurement. Moreover, the BiVO<sub>4</sub> thin layer has uniform thickness by electrodeposition with pulsed voltage. As a result, most of the photo-generated electron-hole pairs are produced near the nanorod/electrolyte interface regardless of the direction of illumination.<sup>38</sup>

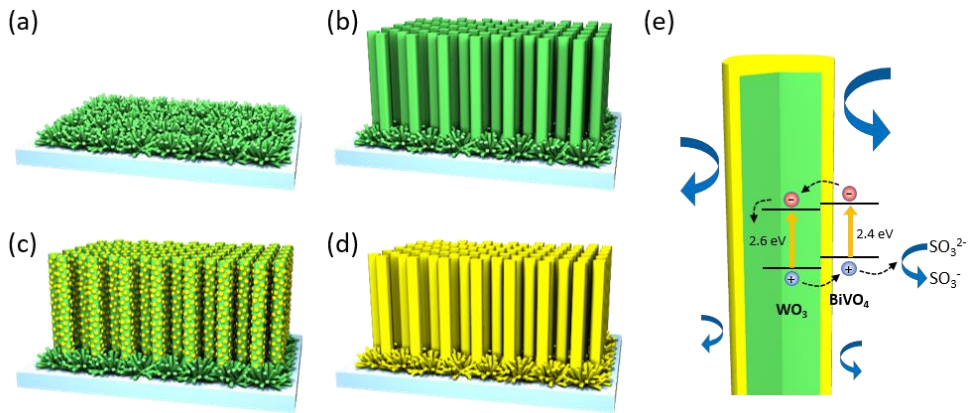


**Figure 2.18** Schematic illustration of produced photoanodes. (a, b)  $WO_3$  nanorods synthesized by hydrothermal method for (a) 30 minutes and (b) 4 hours. (c, d)  $WO_3/BVO$  hetero-nanostructure produced by hydrothermal and electrodeposition method. Pulsed electrodeposition was performed (c) 6 cycles and (d) 9 cycles. (e) Cross-section view of core-shell nanostructure.

Although the electrons should travel from the interface to the current collector, they can quickly move owing to the good transport property of  $\text{WO}_3$  and nanorod structure. Also, core-shell structure lets  $\text{BiVO}_4$  with small band gap absorb wider range of light in advance so that all photo-generation and oxidation of water occurs by  $\text{BiVO}_4$  layer as shown in Figure 2.18e.

Table 2.4 shows various methods and nanostructures reported for  $\text{WO}_3/\text{BiVO}_4$  photoanodes and their PEC performance. It can be seen that the photocurrent density of our  $\text{WO}_3/\text{BiVO}_4$  photoanode is comparable to the other works considering the high stability, front illumination, and all-solution process.

**Table 2.4** PEC performance of the reported WO<sub>3</sub>/BiVO<sub>4</sub> photoanodes.

Ref.	Method	All-solution process	Morphology	Photocurrent density (vs. RHE)	Direction of incident light	Long-term stability
25	Polymer-assisted direct deposition	Yes	Porous film	0.75 mA/cm <sup>2</sup> (0.5 M Na <sub>2</sub> SO <sub>4</sub> + 0.05 M Methanol)	Front	-
36	Spin coating	Yes	Planar film	0.8 mA/cm <sup>2</sup> (0.5 M Na <sub>2</sub> SO <sub>4</sub> )	Back	-
	Solvothermal method	Yes	Nanorods	1.6 mA/cm <sup>2</sup> (0.5 M Na <sub>2</sub> SO <sub>4</sub> )	Back	Stable
35	Glancing angle deposition / Electrodeposition	No	Nanorods	5.45 mA/cm <sup>2</sup> (KPi (pH 7))	45 °	-
31	Glancing angle deposition / Pulsed electrodeposition	No	Nanorods	4.55 mA/cm <sup>2</sup> (0.5 M KPi + 1 M Na <sub>2</sub> SO <sub>3</sub> (pH 7.2))	Back	-
62	Hydrothermal method	Yes	Nanorods	0.5 mA/cm <sup>2</sup> (0.5 M Na <sub>2</sub> SO <sub>4</sub> )	-	-
37	Sol-gel / Electrodeposition	Yes	Inverse opals	0.8 mA/cm <sup>2</sup> (0.5 M Na <sub>2</sub> SO <sub>4</sub> )	Back	-
22	Hydrothermal method / Spin coating	Yes	Nanoplates	3.9 mA/cm <sup>2</sup> (0.1 M Na <sub>2</sub> SO <sub>4</sub> )	Front	Unstable
56	Solvothermal method / Drop casting	Yes	Yolk-shell	2.3 mA/cm <sup>2</sup> (0.5 M Na <sub>2</sub> SO <sub>4</sub> )	Back	Stable
This work	Hydrothermal / Pulsed electrodeposition	Yes	Nanorods	4.15 mA/cm <sup>2</sup> (0.5 M KPi (pH 7) + 1 M Na <sub>2</sub> SO <sub>3</sub> )	Front	Stable
				3.23 mA/cm <sup>2</sup> (0.5 M KPi (pH 7))	Front	Unstable

## 2.4. Conclusions

In summary, we have successfully synthesized  $\text{WO}_3/\text{BiVO}_4$  core-shell nanostructures on the FTO substrate with high performance by the all-solution process. We optimized the size and density of  $\text{WO}_3$  nanorods by hydrothermal synthesis and the configuration of  $\text{BiVO}_4$  by pulsed electrodeposition for photoanodes. The enhanced photocurrent density of  $4.15 \text{ mA/cm}^2$  at 1.23 V versus RHE and the maximum IPCE of 75.9 % at 430 nm were achieved with the optimized  $\text{WO}_3/\text{BiVO}_4$  heterojunction photoanodes by alleviating the shortcomings of each other without additional catalysts. Owing to the nanostructures of the photoanode, front illumination, which is favorable in practical use, was superior to back illumination. Furthermore, the  $\text{BiVO}_4$  thin film on  $\text{WO}_3$  nanorods acted as a passivation layer, thereby enhancing the stability of the photoanode. We believe that these  $\text{WO}_3/\text{BiVO}_4$  core-shell hetero-nanostructure photoanodes are suitable to be applied to the high-performance tandem PEC devices.

## 2.5. References

1. Turner, J. A., A Realizable Renewable Energy Future. *Science* **1999**, 285, 687-689.
2. Chu, S.; Majumdar, A., Opportunities and challenges for a sustainable energy future. *Nature* **2012**, 488 (7411), 294-303.
3. Bard, A. J.; Fox, M. A., Artificial Photosynthesis: Solar Splitting of Water to Hydrogen and Oxygen. *Acc. Chem. Res.* **1995**, 28, 141-145.
4. Grätzel, M., Photoelectrochemical cells. *Nature* **2001**, 414, 338-344.
5. Bak, T.; Nowotny, J.; Rekas, M.; Sorrell, C. C., Photo-electrochemical hydrogen generation from water using solar energy. Materials-related aspects. *Int. J. Hydrogen Energy* **2002**, 27 (10), 991-1022.
6. Kalanur, S. S.; Hwang, Y. J.; Chae, S. Y.; Joo, O. S., Facile growth of aligned WO<sub>3</sub> nanorods on FTO substrate for enhanced photoanodic water oxidation activity. *J. Mater. Chem. A* **2013**, 1 (10).
7. Zhu, T.; Chong, M. N.; Chan, E. S., Nanostructured tungsten trioxide thin films synthesized for photoelectrocatalytic water oxidation: a review. *ChemSusChem* **2014**, 7 (11), 2974-97.
8. Zhang, T.; Wang, L.; Su, J.; Guo, L., Branched Tungsten Oxide Nanorod Arrays Synthesized by Controlled Phase Transformation for Solar Water Oxidation. *ChemCatChem* **2016**, 8 (12), 2119-2127.

9. Kuang, Y.; Jia, Q.; Nishiyama, H.; Yamada, T.; Kudo, A.; Domen, K., A Front-Illuminated Nanostructured Transparent BiVO<sub>4</sub> Photoanode for >2% Efficient Water Splitting. *Adv. Energy Mater.* **2016**, *6* (2).
10. Jeong, S. Y.; Choi, K. S.; Shin, H. M.; Kim, T. L.; Song, J.; Yoon, S.; Jang, H. W.; Yoon, M. H.; Jeon, C.; Lee, J.; Lee, S., Enhanced Photocatalytic Performance Depending on Morphology of Bismuth Vanadate Thin Film Synthesized by Pulsed Laser Deposition. *ACS Appl. Mater. Interfaces* **2017**, *9* (1), 505-512.
11. Bhat, S. S. M.; Jang, H. W., Recent Advances in Bismuth-Based Nanomaterials for Photoelectrochemical Water Splitting. *ChemSusChem* **2017**, *10* (15), 3001-3018.
12. Sivula, K.; Zboril, R.; Formal, F. L.; Robert, R.; Weidenkaff, A.; Tucek, J.; Frydrych, J.; Grätzel, M., Photoelectrochemical Water Splitting with Mesoporous Hematite Prepared by a Solution-Based Colloidal Approach. *J. Am. Chem. Soc.* **2010**, *132* (21), 7436-7444.
13. Kim do, H.; Andoshe, D. M.; Shim, Y. S.; Moon, C. W.; Sohn, W.; Choi, S.; Kim, T. L.; Lee, M.; Park, H.; Hong, K.; Kwon, K. C.; Suh, J. M.; Kim, J. S.; Lee, J. H.; Jang, H. W., Toward High-Performance Hematite Nanotube Photoanodes: Charge-Transfer Engineering at Heterointerfaces. *ACS Appl. Mater. Interfaces* **2016**, *8* (36), 23793-800.

14. Andoshe, D. M.; Choi, S.; Shim, Y.-S.; Lee, S. H.; Kim, Y.; Moon, C. W.; Kim, D. H.; Lee, S. Y.; Kim, T.; Park, H. K.; Lee, M. G.; Jeon, J.-M.; Nam, K. T.; Kim, M.; Kim, J. K.; Oh, J.; Jang, H. W., A wafer-scale antireflective protection layer of solution-processed TiO<sub>2</sub> nanorods for high performance silicon-based water splitting photocathodes. *J. Mater. Chem. A* **2016**, *4* (24), 9477-9485.
15. Zhang, Z.; Gao, C.; Wu, Z.; Han, W.; Wang, Y.; Fu, W.; Li, X.; Xie, E., Toward efficient photoelectrochemical water-splitting by using screw-like SnO<sub>2</sub> nanostructures as photoanode after being decorated with CdS quantum dots. *Nano Energy* **2016**, *19*, 318-327.
16. Zhou, J.; Lin, S.; Chen, Y.; Gaskov, A. M., Facile morphology control of WO<sub>3</sub> nanostructure arrays with enhanced photoelectrochemical performance. *Appl. Surf. Sci.* **2017**, *403*, 274-281.
17. Baek, J. H.; Kim, B. J.; Han, G. S.; Hwang, S. W.; Kim, D. R.; Cho, I. S.; Jung, H. S., BiVO<sub>4</sub>/WO<sub>3</sub>/SnO<sub>2</sub> Double-Heterojunction Photoanode with Enhanced Charge Separation and Visible-Transparency for Bias-Free Solar Water-Splitting with a Perovskite Solar Cell. *ACS Appl. Mater. Interfaces* **2017**, *9* (2), 1479-1487.
18. Liu, C.; Yang, Y.; Li, J.; Chen, S.; Li, W.; Tang, X., An in situ transformation approach for fabrication of BiVO<sub>4</sub>/WO<sub>3</sub> heterojunction

- photoanode with high photoelectrochemical activity. *Chemical Engineering Journal* **2017**, *326*, 603-611.
19. Chae, S. Y.; Lee, C. S.; Jung, H.; Joo, O. S.; Min, B. K.; Kim, J. H.; Hwang, Y. J., Insight into Charge Separation in WO<sub>3</sub>/BiVO<sub>4</sub> Heterojunction for Solar Water Splitting. *ACS Appl. Mater. Interfaces* **2017**, *9* (23), 19780-19790.
  20. Feng, X.; Chen, Y.; Qin, Z.; Wang, M.; Guo, L., Facile Fabrication of Sandwich Structured WO<sub>3</sub> Nanoplate Arrays for Efficient Photoelectrochemical Water Splitting. *ACS Appl. Mater. Interfaces* **2016**, *8* (28), 18089-96.
  21. Kafizas, A.; Francàs, L.; Sotelo-Vazquez, C.; Ling, M.; Li, Y.; Glover, E.; McCafferty, L.; Blackman, C.; Darr, J.; Parkin, I., Optimizing the Activity of Nanoneedle Structured WO<sub>3</sub> Photoanodes for Solar Water Splitting: Direct Synthesis via Chemical Vapor Deposition. *J. Phys. Chem. C* **2017**, *121* (11), 5983-5993.
  22. Kalanur, S. S.; Yoo, I.-H.; Park, J.; Seo, H., Insights into the electronic bands of WO<sub>3</sub>/BiVO<sub>4</sub>/TiO<sub>2</sub>, revealing high solar water splitting efficiency. *J. Mater. Chem. A* **2017**, *5* (4), 1455-1461.
  23. Zhou, Y.; Zhang, L.; Lin, L.; Wygant, B. R.; Liu, Y.; Zhu, Y.; Zheng, Y.; Mullins, C. B.; Zhao, Y.; Zhang, X.; Yu, G., Highly Efficient

- Photoelectrochemical Water Splitting from Hierarchical WO<sub>3</sub>/BiVO<sub>4</sub> Nanoporous Sphere Arrays. *Nano Lett.* **2017**, *17* (12), 8012-8017.
24. Jeon, D.; Kim, N.; Bae, S.; Han, Y.; Ryu, J., WO<sub>3</sub>/Conducting Polymer Heterojunction Photoanodes for Efficient and Stable Photoelectrochemical Water Splitting. *ACS Appl. Mater. Interfaces* **2018**, *10* (9), 8036-8044.
25. Hong, S. J.; Lee, S.; Jang, J. S.; Lee, J. S., Heterojunction BiVO<sub>4</sub>/WO<sub>3</sub> electrodes for enhanced photoactivity of water oxidation. *Energy Environ. Sci.* **2011**, *4* (5), 1781-1787.
26. Zhong, D. K.; Choi, S.; Gamelin, D. R., Near-complete suppression of surface recombination in solar photoelectrolysis by "Co-Pi" catalyst-modified W:BiVO<sub>4</sub>. *J. Am. Chem. Soc.* **2011**, *133* (45), 18370-7.
27. Liu, X.; Wang, F.; Wang, Q., Nanostructure-based WO<sub>3</sub> photoanodes for photoelectrochemical water splitting. *Phys. Chem. Chem. Phys.* **2012**, *14* (22), 7894-911.
28. Cho, I. S.; Chen, Z.; Forman, A. J.; Kim, D. R.; Rao, P. M.; Jaramillo, T. F.; Zheng, X., Branched TiO<sub>2</sub> nanorods for photoelectrochemical hydrogen production. *Nano Lett.* **2011**, *11* (11), 4978-84.
29. Hartmann, P.; Lee, D.-K.; Smarsly, B. M.; Janek, J., Mesoporous TiO<sub>2</sub>: Comparison of Classical Sol-Gel and Nanoparticle Based

- Photoelectrodes for the Water Splitting Reaction. *ACS Nano* **2010**, *4* (6), 3147-3154.
30. Lim, Y. F.; Chua, C. S.; Lee, C. J.; Chi, D., Sol-gel deposited Cu<sub>2</sub>O and CuO thin films for photocatalytic water splitting. *Phys. Chem. Chem. Phys.* **2014**, *16* (47), 25928-34.
31. Lee, M. G.; Kim, D. H.; Sohn, W.; Moon, C. W.; Park, H.; Lee, S.; Jang, H. W., Conformally coated BiVO<sub>4</sub> nanodots on porosity-controlled WO<sub>3</sub> nanorods as highly efficient type II heterojunction photoanodes for water oxidation. *Nano Energy* **2016**, *28*, 250-260.
32. Musselman, K. P.; Marin, A.; Wisnet, A.; Scheu, C.; MacManus-Driscoll, J. L.; Schmidt-Mende, L., A Novel Buffering Technique for Aqueous Processing of Zinc Oxide Nanostructures and Interfaces, and Corresponding Improvement of Electrodeposited ZnO-Cu<sub>2</sub>O Photovoltaics. *Adv. Funct. Mater.* **2011**, *21* (3), 573-582.
33. Zhang, M.; Zhu, Y.; Li, W.; Wang, F.; Li, H.; Liu, X.; Zhang, W.; Ren, C., Double Z-scheme system of silver bromide@bismuth tungstate/tungsten trioxide ternary heterojunction with enhanced visible-light photocatalytic activity. *J. Colloid Interface Sci.* **2018**, *509*, 18-24.
34. Wu, X.; Yao, S., Flexible electrode materials based on WO<sub>3</sub> nanotube bundles for high performance energy storage devices. *Nano Energy* **2017**, *42*, 143-150.

35. Pihosh, Y.; Turkevych, I.; Mawatari, K.; Uemura, J.; Kazoe, Y.; Kosar, S.; Makita, K.; Sugaya, T.; Matsui, T.; Fujita, D.; Tosa, M.; Kondo, M.; Kitamori, T., Photocatalytic generation of hydrogen by core-shell  $\text{WO}_3/\text{BiVO}_4$  nanorods with ultimate water splitting efficiency. *Sci Rep* **2015**, *5*, 11141.
36. Su, J.; Guo, L.; Bao, N.; Grimes, C. A., Nanostructured  $\text{WO}_3/\text{BiVO}_4$  heterojunction films for efficient photoelectrochemical water splitting. *Nano Lett.* **2011**, *11* (5), 1928-1933.
37. Zhang, H.; Zhou, W.; Yang, Y.; Cheng, C., 3D  $\text{WO}_3/\text{BiVO}_4$ /Cobalt Phosphate Composites Inverse Opal Photoanode for Efficient Photoelectrochemical Water Splitting. *Small* **2017**, *13* (16).
38. Zhou, L.; Zhao, C.; Giri, B.; Allen, P.; Xu, X.; Joshi, H.; Fan, Y.; Titova, L. V.; Rao, P. M., High Light Absorption and Charge Separation Efficiency at Low Applied Voltage from Sb-Doped  $\text{SnO}_2/\text{BiVO}_4$  Core/Shell Nanorod-Array Photoanodes. *Nano Lett.* **2016**, *16* (6), 3463-74.
39. Shi, X.; Jeong, H.; Oh, S. J.; Ma, M.; Zhang, K.; Kwon, J.; Choi, I. T.; Choi, I. Y.; Kim, H. K.; Kim, J. K.; Park, J. H., Unassisted Photoelectrochemical Water Splitting Exceeding 7% Solar-to-Hydrogen Conversion Efficiency Using Photon Recycling. *Nat Commun* **2016**, *7*, 11943.

40. Lee, S. A.; Lee, T. H.; Kim, C.; Lee, M. G.; Choi, M.-J.; Park, H.; Choi, S.; Oh, J.; Jang, H. W., Tailored NiO<sub>x</sub>/Ni Cocatalysts on Silicon for Highly Efficient Water Splitting Photoanodes via Pulsed Electrodeposition. *ACS Catalysis* **2018**, *8* (8), 7261-7269.
41. Bhat, S. S. M.; Suh, J. M.; Choi, S.; Hong, S.-P.; Lee, S. A.; Kim, C.; Moon, C. W.; Lee, M. G.; Jang, H. W., Substantially Enhanced Front Illumination Photocurrent in Porous SnO<sub>2</sub> Nanorods/Networked BiVO<sub>4</sub> Heterojunction Photoanodes. *J. Mater. Chem. A* **2018**, *6* (30), 14633-14643.
42. Andoshe, D. M.; Jin, G.; Lee, C.-S.; Kim, C.; Kwon, K. C.; Choi, S.; Sohn, W.; Moon, C. W.; Lee, S. H.; Suh, J. M.; Kang, S.; Park, J.; Heo, H.; Kim, J. K.; Han, S.; Jo, M.-H.; Jang, H. W., Directly Assembled 3D Molybdenum Disulfide on Silicon Wafer for Efficient Photoelectrochemical Water Reduction. *Advanced Sustainable Systems* **2018**, *2* (3), 1700142.
43. Kim, T. W.; Choi, K.-S., Nanoporous BiVO<sub>4</sub> photoanodes with dual-layer oxygen evolution catalysts for solar water splitting. *Science* **2014**, *343* (6174), 990-994.
44. Chae, S. Y.; Jung, H.; Jeon, H. S.; Min, B. K.; Hwang, Y. J.; Joo, O.-S., Morphology Control of One-Dimensional Heterojunctions for Highly

- Efficient Photoanodes Used for Solar Water Splitting. *J. Mater. Chem. A* **2014**, 2 (29).
45. Jelinska, A.; Bienkowski, K.; Jadwiszczak, M.; Pisarek, M.; Strawski, M.; Kurzydowski, D.; Solarska, R.; Augustynski, J., Enhanced Photocatalytic Water Splitting on Very Thin WO<sub>3</sub> Films Activated by High-Temperature Annealing. *ACS Catalysis* **2018**, 8 (11), 10573-10580.
  46. Ma, Z.; Song, K.; Wang, L.; Gao, F.; Tang, B.; Hou, H.; Yang, W., WO<sub>3</sub>/BiVO<sub>4</sub> Type-II Heterojunction Arrays Decorated with Oxygen-deficient ZnO Passivation Layer: a Highly Efficient and Stable Photoanode. *ACS Appl. Mater. Interfaces* **2018**.
  47. Cen, J.; Wu, Q.; Yan, D.; Zhang, W.; Zhao, Y.; Tong, X.; Liu, M.; Orlov, A., New Aspects of Improving The Performance of WO<sub>3</sub> Thin Films for Photoelectrochemical Water Splitting by Tuning The Ultrathin Depletion Region. *RSC Advances* **2019**, 9 (2), 899-905.
  48. Soltani, T.; Tayyebi, A.; Hong, H.; Mirfasih, M. H.; Lee, B.-K., A Novel Growth Control of Nanoplates WO<sub>3</sub> Photoanodes with Dual Oxygen and Tungsten Vacancies for Efficient Photoelectrochemical Water Splitting Performance. *Sol. Energ. Mat. Sol. C.* **2019**, 191, 39-49.
  49. Wang, Y.; Tian, W.; Chen, L.; Cao, F.; Guo, J.; Li, L., Three-Dimensional WO<sub>3</sub> Nanoplate/Bi<sub>2</sub>S<sub>3</sub> Nanorod Heterojunction as a Highly

- Efficient Photoanode for Improved Photoelectrochemical Water Splitting. *ACS Appl. Mater. Interfaces* **2017**, *9* (46), 40235-40243.
50. Wang, L.; Wang, W.; Chen, Y.; Yao, L.; Zhao, X.; Shi, H.; Cao, M.; Liang, Y., Heterogeneous p-n Junction CdS/Cu<sub>2</sub>O Nanorod Arrays: Synthesis and Superior Visible-Light-Driven Photoelectrochemical Performance for Hydrogen Evolution. *ACS Appl. Mater. Interfaces* **2018**, *10* (14), 11652-11662.
51. Li, Y. Y.; Wang, J. G.; Sun, H. H.; Wei, B., Heterostructured TiO<sub>2</sub>/NiTiO<sub>3</sub> Nanorod Arrays for Inorganic Sensitized Solar Cells with Significantly Enhanced Photovoltaic Performance and Stability. *ACS Appl. Mater. Interfaces* **2018**, *10* (14), 11580-11586.
52. Zhang, Y.; Guo, Y.; Duan, H.; Li, H.; Sun, C.; Liu, H., Facile Synthesis of V<sup>4+</sup> Self-Doped, [010] Oriented BiVO<sub>4</sub> Nanorods with Highly Efficient Visible Light-Induced Photocatalytic Activity. *Phys Chem Chem Phys* **2014**, *16* (44), 24519-24526.
53. Seabold, J. A.; Choi, K.-S., Effect of a Cobalt-Based Oxygen Evolution Catalyst on the Stability and the Selectivity of Photo-Oxidation Reactions of a WO<sub>3</sub> Photoanode. *Chemistry of Materials* **2011**, *23* (5), 1105-1112.

54. Lee, D. K.; Choi, K.-S., Enhancing Long-Term Photostability of BiVO<sub>4</sub> Photoanodes for Solar Water Splitting by Tuning Electrolyte Composition. *Nature Energy* **2017**, *3* (1), 53-60.
55. Pilli, S. K.; Janarthanan, R.; Deutsch, T. G.; Furtak, T. E.; Brown, L. D.; Turner, J. A.; Herring, A. M., Efficient photoelectrochemical water oxidation over cobalt-phosphate (Co-Pi) catalyst modified BiVO<sub>4</sub>/1D-WO<sub>3</sub> heterojunction electrodes. *Phys Chem Chem Phys* **2013**, *15* (35), 14723-8.
56. Jin, B.; Jung, E.; Ma, M.; Kim, S.; Zhang, K.; Kim, J. I.; Son, Y.; Park, J. H., Solution-processed yolk-shell-shaped WO<sub>3</sub>/BiVO<sub>4</sub> heterojunction photoelectrodes for efficient solar water splitting. *Journal of Materials Chemistry A* **2018**, *6* (6), 2585-2592.
57. Lamm, B.; Trzeźniowski, B. J.; Döscher, H.; Smith, W. A.; Stefik, M., Emerging Postsynthetic Improvements of BiVO<sub>4</sub> Photoanodes for Solar Water Splitting. *ACS Energy Letters* **2017**, *3* (1), 112-124.
58. Toma, F. M.; Cooper, J. K.; Kunzelmann, V.; McDowell, M. T.; Yu, J.; Larson, D. M.; Borys, N. J.; Abelyan, C.; Beeman, J. W.; Yu, K. M.; Yang, J.; Chen, L.; Shaner, M. R.; Spurgeon, J.; Houle, F. A.; Persson, K. A.; Sharp, I. D., Mechanistic Insights into Chemical and Photochemical Transformations of Bismuth Vanadate Photoanodes. *Nat Commun* **2016**, *7*, 12012.

59. Zhang, Z.; Li, Y.; Jiang, X.; Han, W.; Xie, M.; Wang, F.; Xie, E., Significantly Improved Charge Collection and Interface Injection in 3D BiVO<sub>4</sub> Based Multilayered Core-Shell Nanowire Photocatalysts. *Nanoscale* **2017**, *9* (37), 14015-14022.
60. Shi, X.; Choi, I. Y.; Zhang, K.; Kwon, J.; Kim, D. Y.; Lee, J. K.; Oh, S. H.; Kim, J. K.; Park, J. H., Efficient photoelectrochemical hydrogen production from bismuth vanadate-decorated tungsten trioxide helix nanostructures. *Nature Communications* **2014**, *5*, 4775.
61. Wang, S.; He, T.; Yun, J.-H.; Hu, Y.; Xiao, M.; Du, A.; Wang, L., New Iron-Cobalt Oxide Catalysts Promoting BiVO<sub>4</sub> Films for Photoelectrochemical Water Splitting. *Advanced Functional Materials* **2018**, *28* (34).
62. Iqbal, N.; Khan, I.; Yamani, Z. H. A.; Qurashi, A., A facile one-step strategy for in-situ fabrication of WO<sub>3</sub>-BiVO<sub>4</sub> nanoarrays for solar-driven photoelectrochemical water splitting applications. *Solar Energy* **2017**, *144*, 604-611.

## **Chapter 3**

### **Co-doped $\text{In}_2\text{S}_3/\text{In}_2\text{O}_3$ Photoanodes for Efficient Photoelectrochemical Water Splitting**

### 3.1. Introduction

As the interest in sustainable energy production increases, water splitting through semiconductor materials to convert solar energy directly to hydrogen energy has been extensively reported to date. Recently, the III–VI group chalcogenide semiconductors, which have good mechanical and thermal stability, have received great attention for narrow-gap photoelectrochemical (PEC) water splitting electrodes.<sup>1</sup> Among the metal sulfides,  $\text{In}_2\text{S}_3$  with narrow band gap of 2.0–2.3 eV has attracted great interest for various applications recently.<sup>2</sup> Owing to its high photoelectric sensitivity, high photoconductivity, large photoelectric conversion yield, low toxicity, and high absorption coefficient,<sup>3–5</sup>  $\text{In}_2\text{S}_3$  shows superior properties in optical-absorption applications such as photoanodes,<sup>2, 6–12</sup> photocatalysts,<sup>3, 13–20</sup> solar cells,<sup>21</sup> photocatalytic conversion of carbon dioxide ( $\text{CO}_2$ ) reduction,<sup>22–23</sup> electrochemical storage cells,<sup>24</sup> and photodetectors.<sup>4, 25–26</sup>

Nevertheless, since the photoelectrochemical properties of  $\text{In}_2\text{S}_3$  were reported by Becker et al. in 1986 for the first time,<sup>27</sup> the researches on  $\text{In}_2\text{S}_3$ -based photoelectrodes have been rarely reported. In fact, despite the superior advantages, there is a serious problem of photocorrosion induced by accumulated holes on the surface of the electrodes during the photocatalytic reaction under illumination which reduces the PEC properties. However, on

account of its unique electrical and optical properties,  $\beta$ - $\text{In}_2\text{S}_3$ -based photoelectrodes have been attracted a renewed interest lately.

### 3.1.1. Crystal Structures of $\text{In}_2\text{S}_3$

$\text{In}_2\text{S}_3$  exists in three stable phases:  $\alpha$ - $\text{In}_2\text{S}_3$  with defective cubic structure,  $\beta$ - $\text{In}_2\text{S}_3$  with defective spinel structure, and  $\gamma$ - $\text{In}_2\text{S}_3$  with layered hexagonal structure, where other two phases ( $\epsilon$ - and  $\text{Th}_3\text{P}_4$ -  $\text{In}_2\text{S}_3$ ) are instable in an ambient pressure.<sup>5, 12, 28-29</sup>  $\beta$ - $\text{In}_2\text{S}_3$  can be further divided into cubic or tetragonal phase.<sup>30</sup> The tetragonal  $\beta$ - $\text{In}_2\text{S}_3$  is the room temperature phase which is stable up to 420 °C. Above 420 °C, the cubic  $\alpha$ - $\text{In}_2\text{S}_3$  and the cubic  $\beta$ - $\text{In}_2\text{S}_3$  appear with disordering of the tetrahedral vacancies. Above 750 °C, the hexagonal  $\gamma$ - $\text{In}_2\text{S}_3$  is stable.<sup>29</sup> However, the high-temperature cubic  $\alpha$ - and  $\beta$ - phases can be obtained by wet chemical methods at low temperature with indium (In)/sulfur (S) ratio control.<sup>29</sup>

Among the three different stable phases,  $\beta$ - $\text{In}_2\text{S}_3$  is the most favorable structure for many applications with its natural defects in the crystal.<sup>4</sup>  $\beta$ - $\text{In}_2\text{S}_3$  is considered as a quasi-ternary compound of In, S, and vacancies.<sup>4</sup> In  $\beta$ - $\text{In}_2\text{S}_3$  crystal, indium ion ( $\text{In}^{3+}$ ) centers are surrounded by six sulfur anions ( $\text{S}^{2-}$ ) in the octahedral sites and four  $\text{S}^{2-}$  anions in the tetrahedral sites. The octahedral sites are fully occupied with cation centers while the 2/3 of tetrahedral sites are occupied and 1/3 of them are empty forming the  $\text{In}^{3+}$  vacancies.<sup>5</sup> The

neighboring sulfur atoms would be bonded to three indium atoms rather than four as usual.<sup>31</sup> The existence of vacancies results in the exhibition of electron affinity and the vacancies act as electron traps. Also, these vacancies make a small distortion from the regular spinel structure. As a defective spinel structure, the structure of  $\beta$ - $\text{In}_2\text{S}_3$  (cubic or tetragonal) is determined by the arrangement of cation vacancies.<sup>29, 32</sup> The ordering of vacancies at tetrahedral cation sites results in a tetragonal structure while the randomly ordering (disordering) of vacancies results in a cubic structure. Interestingly, most of its unique properties come from the defective spinel crystal structure.

### **3.1.2. $\text{In}_2\text{S}_3$ : Promising Material for Photoelectrodes**

Among the various metal sulfides,  $\beta$ - $\text{In}_2\text{S}_3$  is regarded as a potential candidate recently in photocatalytic applications due to the less environmental and health concerns, high photoelectric sensitivity, moderate charge transport, and high photoconductivity as briefly mentioned above.<sup>4, 33-34</sup> Already in the field of solar cells,  $\text{In}_2\text{S}_3$  received a great attention as an alternative to the cadmium sulfide (CdS) buffer layer which contains harmful element, cadmium (Cd), in the material.<sup>21</sup> Since the visible light occupies the large proportion in the solar spectrum (~ 46 %), the semiconductors with narrow band gap like  $\beta$ - $\text{In}_2\text{S}_3$  is beneficial for photoelectrochemical cells.<sup>12</sup>

$\beta$ - $\text{In}_2\text{S}_3$  has an indirect band gap of 2.0-2.3 eV, with the appropriate band positions for spontaneous water reduction and oxidation reactions, whereas  $\beta$ - $\text{In}_2\text{S}_3$  can only be used as photoanodes rather than photocathodes because it is always an n-type semiconductor.<sup>2</sup> Compared to the semiconductor materials that have been widely used for PEC photoanodes such as  $\text{TiO}_2$ ,  $\text{WO}_3$ , and  $\text{BiVO}_4$ ,  $\beta$ - $\text{In}_2\text{S}_3$  can absorb wider range of light up to 540-620 nm. Since the position of  $E_{\text{CB}}$  is relatively negative, it is feasible to construct type II heterostructures with various materials.<sup>34</sup> Furthermore, its band gap can be adjusted through the quantum confinement effect owing to the large exciton Bohr diameter of 33.8 nm.<sup>2</sup>

The high absorption coefficient, large photoelectric conversion yield, and high photoconductivity of  $\text{In}_2\text{S}_3$  are attributed to the defects from indium vacancies in the crystal. Its high defect density induces a lot of imperfection states in the material. These trap states or intermediate band within the band gap allow the absorption of surplus energy of photo-excited electrons and holes and the excitation of another charge carriers as well as the absorption of lower-energy photons.<sup>35</sup> Also, the defect structure of  $\beta$ - $\text{In}_2\text{S}_3$  can generate distorted electric field, resulting in effective charge separation.<sup>13, 33</sup>

There are some reports that  $\beta$ - $\text{In}_2\text{S}_3$  with cubic structure is beneficial for photocatalytic reaction because of the disordered indium vacancies.<sup>32, 34</sup> Fu *et al.* proposed that sulfur-bridged indium ions in  $\text{In}_2\text{S}_3$  crystal structure offer as

charge transport pathways of charge carriers to move from the interior of the material to the surface.<sup>32</sup> Unfortunately, the ordered vacancies in the tetragonal structure of  $\beta$ - $\text{In}_2\text{S}_3$  might depress the transport efficiency resulting in the recombination before the photo-excited charge carriers reach to the surface for water oxidation. Meanwhile, the cubic structured  $\beta$ - $\text{In}_2\text{S}_3$  with disordered vacancies would not provide this type of defects.

### **3.1.3. Limitations of $\text{In}_2\text{S}_3$ as Photoelectrodes**

Metal sulfides, however, usually suffer from photocorrosion in aqueous solution during the photocatalytic reaction.<sup>19</sup> On the surface of metal sulfides under illumination, sluggish oxidation reaction occurs and the photo-generated holes transported to the surface of the material are accumulated. These accumulated holes weaken the In-S bond or attack  $\text{S}^{2-}$  ions and then oxidize the surface of material rather than water molecules inducing the decomposition of sulfide materials into soluble sulfates.<sup>33, 36-37</sup> Besides, the photo-induced ions can be adsorbed on the surface occupying the active sites and shielding the light absorption.<sup>19</sup> Because of its photo-corrosive property, numerous efforts have been devoted for  $\text{In}_2\text{S}_3$ -based applications to prevent the undesired degradation. For example, nickel oxide hydroxide ( $\text{NiOOH}$ ) co-catalyst was attached to  $\text{CdS}/\text{In}_2\text{S}_3$  photoanodes to avoid direct contact between electrolyte and the photoanodes and to promote oxygen production

with accumulated holes on the surface of sulfides.<sup>38</sup> Also, controlling nanostructures of  $\text{In}_2\text{S}_3$ -based heterojunction helped to consume photoexcited holes efficiently.<sup>33</sup> As a result, the photoanodes with adjusted amount of  $\text{In}_2\text{S}_3$  showed much better photostability.

Furthermore, for sufficient light absorption, porous 1D to 3D nanostructures vertically grown on a substrate such as nanorods, nanotubes, nanoplates, and nanotrees with thickness of several micrometers are usually required.<sup>39-40</sup> However, it is hard to form these nanostructures by  $\text{In}_2\text{S}_3$  itself. To achieve those nanostructures with extensive active area and sufficient amount of the material, the supporting nanostructures of other materials should be used additionally.<sup>33</sup> Otherwise, the bulk  $\text{In}_2\text{S}_3$  film with the thickness of several micrometers would cause the recombination of photo-generated electrons and holes before the charge carriers reach to the surface of each electrodes for water redox reaction. Accordingly, there are various strategies to overcome these limitations of  $\text{In}_2\text{S}_3$  as photoanodes including nanostructure morphology control, constructing type II heterojunction, surface passivation, deposition of co-catalyst, and metal ion doping. Herein, the PEC properties of  $\text{In}_2\text{S}_3$  was improved by constructing type II heterostructures with vertically grown  $\text{In}_2\text{O}_3$  nanorods on the substrates. The heteronanostructures with large surface area provide the photoactive sites for water splitting and facilitate the light absorption and charge separation of photo-generated electrons and

holes.<sup>41</sup> Additionally, cobalt ions were doped into  $\text{In}_2\text{S}_3$  for further improvement. The charge transfer efficiency and light absorption were enhanced by increased surface area and carrier density. We believe that our study on the integration of several strategies for efficient PEC water splitting using  $\text{In}_2\text{S}_3$  would provide the motivation to researchers for further improvement of  $\text{In}_2\text{S}_3$ -based photoanodes, which has not been explored considerably.

### **3.3. Experimental Details**

#### **3.3.1. Preparation of $\text{In}_2\text{O}_3$ Nanorods**

$\text{In}_2\text{O}_3$  nanorods were synthesized by glancing angle deposition (GLAD) on a fluorine doped tin oxide (FTO) substrate.  $\text{In}_2\text{O}_3$  powder (Kojundo Co.) was poured in a carbon crucible and placed in the e-beam evaporator. Prior to the  $\text{In}_2\text{O}_3$  nanorods deposition, a thin  $\text{In}_2\text{O}_3$  film (~50 nm) was deposited to improve the adhesion between the substrate and the nanostructures. The substrate was continuously rotated at speed of 80 rpm during the deposition with the glancing angle of  $85^\circ$  to form  $\text{In}_2\text{O}_3$  nanorod arrays. The pressure in the chamber was maintained under  $4.0 \times 10^{-5}$  Torr. The as-deposited samples were transformed to crystalline phase by annealing at  $500^\circ\text{C}$  for 2 h in air. GLAD technique enables the thickness and morphology control of nanostructures with high reproducibility. Moreover, GLAD with a constant

rotation speed results in the formation of well-separated and vertically aligned  $\text{In}_2\text{O}_3$  nanorods.

### **3.3.2. Preparation of $\text{In}_2\text{O}_3/\text{In}_2\text{S}_3$ and $\text{In}_2\text{O}_3/\text{Co}$ Doped $\text{In}_2\text{S}_3$ Heterostructures**

Indium chloride ( $\text{InCl}_3$ , 0.015 M), 250 mg of thioacetamide, and 700 mg of citric acid were dissolved in 50 ml of distilled (DI) water. The citric acid was used as a complexing agent to compress the activity of indium (In) ions and adjust the pH of the reaction solution.<sup>42</sup> The  $\text{In}_2\text{O}_3$  nanorods coated FTO substrates were dipped in the  $\text{InCl}_3$  precursor solution at 80 °C for 1 h under vigorous stirring condition. The samples were taken out from the beaker, washed with distilled water to remove excess material on the surface, and then dried at 60 °C overnight in air. Co-doped  $\text{In}_2\text{S}_3$  layer was synthesized on  $\text{In}_2\text{O}_3$  nanorods by following the same procedure with addition of different mol% (3, 5, and 7%) of cobalt chloride.

### **3.3.3. Characterization**

The morphology of pristine  $\text{In}_2\text{O}_3$  nanorods and the  $\text{In}_2\text{O}_3/\text{In}_2\text{S}_3$  heterojunction nanostructures was investigated by a field-emission scanning electron microscope (FESEM, Zeiss, MERLIN Compact). Transmission electron microscope (TEM, JEOL JEM 3000F) analysis was

conducted to characterize the nanostructures of  $\text{In}_2\text{O}_3/\text{Co-In}_2\text{S}_3$  heterojunctions. The crystalline phase of pristine  $\text{In}_2\text{O}_3$ ,  $\text{In}_2\text{O}_3/\text{In}_2\text{S}_3$ , and  $\text{In}_2\text{O}_3/\text{Co-In}_2\text{S}_3$  nanorods was determined by X-ray diffractometry (XRD, Bruker, D8-ADVANCE). The transmittance (T) and reflectance (R) of  $\text{In}_2\text{O}_3$ ,  $\text{In}_2\text{O}_3/\text{In}_2\text{S}_3$ , and  $\text{In}_2\text{O}_3/\text{Co-In}_2\text{S}_3$  nanorods were determined by UV-vis characterization to calculate absorptance (1-T-R).

### 3.3.4. PEC Measurement

All the PEC data was collected by a potentiostat (Ivium Technologies, Nstat) using a three-electrode system. The prepared sample was used as the working electrode, Ag/AgCl/saturated KCl as the reference electrode, and a Pt wire as the counter electrode. The potentials versus Ag/AgCl were converted to the RHE using the Nernst relation:  $E_{\text{RHE}} = E_{\text{Ag/AgCl}}^0 + E_{\text{Ag/AgCl}} + 0.059 \times \text{pH}$ , where  $E_{\text{RHE}}$  is the converted potential versus RHE, the reference potential of Ag/AgCl,  $E_{\text{Ag/AgCl}}^0$ , is 0.198 V, and  $E_{\text{Ag/AgCl}}$  is the measured potentials against RHE and Ag/AgCl. For the electrolyte, 0.5 M  $\text{Na}_2\text{SO}_4$  solution was used. Linear sweep voltammetry (LSV) measurements were performed at a scan rate of 10 mV/s under AM 1.5G simulated solar light illumination which was calibrated to 1 sun ( $100 \text{ mW}/\text{cm}^2$ ) using the reference cell. Electrochemical impedance spectroscopy (EIS) spectra were collected in the same three-electrode system sweeping 100 kHz to 0.1 Hz with an ac amplitude of 10 mV

and fitted using the ZsimpWin software. The LSV measurement in 0.5 M Na<sub>2</sub>SO<sub>4</sub> with 0.5 M Na<sub>2</sub>SO<sub>3</sub> as hole scavenger were conducted to calculate the charge transfer efficiency ( $\eta_{trans}$ ) at the electrode/electrolyte interface:

$$J_{H_2O} = J_{max} \times \eta_{abs} \times \eta_{trans} \times \eta_{sep}$$

$$J_{Na_2SO_3} = J_{max} \times \eta_{abs} \times \eta_{sep}$$

where  $J_{H_2O}$  is the measured photocurrent density for water oxidation,  $J_{max}$  is the theoretical maximum photocurrent, and  $\eta_{abs}$  is the light absorption efficiency. Assuming that the charge transfer efficiency is 100% in the Na<sub>2</sub>SO<sub>3</sub> solution, we can calculate the charge transfer efficiency at the semiconductor/electrolyte interface by dividing the photocurrent density for water oxidation by that for sulfite oxidation.

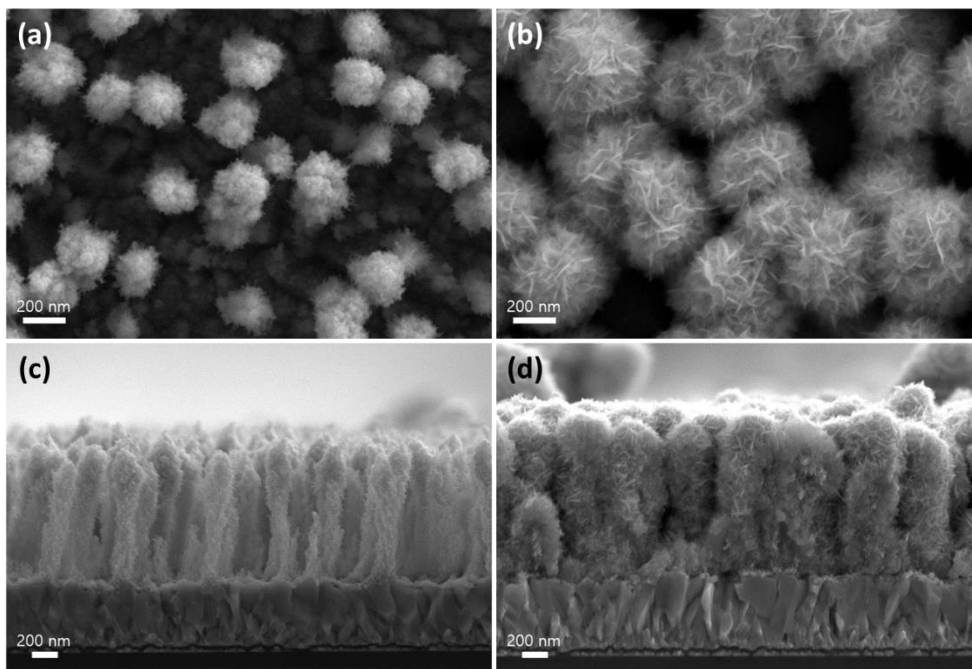


**Figure 3.1** Top and cross-section SEM images of pristine  $\text{In}_2\text{O}_3$  and  $\text{In}_2\text{O}_3/\text{In}_2\text{S}_3$  heterostructures grown on the FTO substrates.

### 3.4. Results and Discussion

$\text{In}_2\text{O}_3$  nanorods as the supporting nanostructures for outer  $\text{In}_2\text{S}_3$  layer were formed by GLAD technique on FTO substrates. GLAD is a facile thermal evaporation method to deposit columnar nanostructures with almost no restriction on materials. The substrate is placed at a large tilted angle against the incident vapor flux with continuous rotation. The material forms uniform nanorods rather than compact thin film owing to the shadowing effect.<sup>43</sup> As the atoms are evaporated and nucleate on the substrate, vapor cannot reach to the region behind the nucleus and can only be deposited on the islands to grow columnar structure. This self-assembly growth mechanism enables facile one-step fabrication of nano-column array. By changing the tilting angle and the deposition time, the porosity and thickness of the nanostructures can be controlled, respectively.<sup>44</sup> The  $\text{In}_2\text{O}_3$  nanorods were deposited at glancing angle of  $85^\circ$  to obtain porous structure. Figure 3.1a and c shows the SEM images of vertically grown  $\text{In}_2\text{O}_3$  nanorods on a FTO substrate. To improve the adhesion between  $\text{In}_2\text{O}_3$  nanorods and FTO substrate, the thin  $\text{In}_2\text{O}_3$  film was deposited at the first stage of the deposition. This thin layer that covers the entire surface of FTO with the thickness of 50 nm also prevent charge loss at the interface of FTO glass/electrolyte by avoiding electron back injection into electrolyte and reducing interfacial recombination.<sup>45</sup>  $\text{In}_2\text{O}_3/\text{In}_2\text{S}_3$  heterostructures were synthesized by depositing  $\text{In}_2\text{S}_3$  layer by CBD method

on the vertically grown  $\text{In}_2\text{O}_3$  nanorods as shown in Figure 3.1b and d.  $\text{In}_2\text{S}_3$  was conformally coated on the surface of  $\text{In}_2\text{O}_3$  nanorods. Chemical bath deposition (CBD) is one of the most frequently used methods to synthesize uniform  $\text{In}_2\text{S}_3$  layer on plain substrates and nanostructures. CBD method enables uniform thin film deposition with high quality by uniform intermixing and heating of bath solution.<sup>21</sup> Also, the stoichiometry of the film can be controlled by reactive concentrations.<sup>46</sup> In a synthesis process,  $\text{InCl}_3$ , thioacetamide, and citric acid were used as indium source, sulfur source, and a complexing agent, respectively. The citric acid reduces the activity of  $\text{In}$  ions and adjust the pH of the solution.<sup>46</sup> In the mixed solution of  $\text{InCl}_3$  and thioacetamide (TA),  $\text{In}^{3+}$  ions that are released slowly from  $\text{InCl}_3$  form a variety of complexes. As the reaction temperature increases, TA is hydrolyzed into hydrogen sulfide ( $\text{H}_2\text{S}$ ) and then ionized to  $\text{S}^{2-}$ . Simultaneously, the complexes are hydrolyzed into  $\text{In}^{3+}$  ions. Finally,  $\text{S}^{2-}$  and  $\text{In}^{3+}$  are connected to form  $\text{In}_2\text{S}_3$  nanocrystals.<sup>47</sup>

XRD patterns of pristine  $\text{In}_2\text{O}_3$  and  $\text{In}_2\text{O}_3/\text{In}_2\text{S}_3$  heterostructure are shown in Figure 3.2a. Several sharp peaks were observed at  $2\theta=22.5^\circ$ ,  $30.6^\circ$ ,  $35.6^\circ$ ,  $47.3^\circ$ ,  $51.1^\circ$ , and  $60.9^\circ$  corresponding to (211), (222), (400), (431), (440), and (622) planes of cubic phase of  $\text{In}_2\text{O}_3$ , respectively (JCPDS 06-0416) in both pristine  $\text{In}_2\text{O}_3$  and  $\text{In}_2\text{O}_3/\text{In}_2\text{S}_3$  samples. The diffraction peaks at  $27.5^\circ$  and  $47.9^\circ$  correspond to (311) and (440) plane of cubic  $\beta\text{-In}_2\text{S}_3$  (JCPDS 32-0456),

respectively. It is known that the cubic structured  $\beta$ - $\text{In}_2\text{S}_3$  with disordered vacancies is beneficial for photoelectrodes as mentioned above.

The linear sweep voltammetry curves of pristine  $\text{In}_2\text{S}_3$ , pristine  $\text{In}_2\text{O}_3$ , and  $\text{In}_2\text{O}_3/\text{In}_2\text{S}_3$  nanostructures photoanodes were measured as shown in Figure 3.2b. The photocurrent densities of pristine  $\text{In}_2\text{O}_3$  and pristine  $\text{In}_2\text{S}_3$  are negligible under 0.8 V vs. RHE. On the other hand, the  $\text{In}_2\text{O}_3/\text{In}_2\text{S}_3$  heterostructures exhibited the considerable cathodic onset potential shift as well as the increased photocurrent density compared to those pristine samples in 0.5 M  $\text{Na}_2\text{SO}_4$  solution under illumination. This result is attributed to the narrow band gap of  $\text{In}_2\text{S}_3$  and the construction of heterostructures that facilitates the charge separation within the electrodes. The inset in Figure 3.2b shows the photograph of synthesized pristine  $\text{In}_2\text{S}_3$ ,  $\text{In}_2\text{O}_3$ , and  $\text{In}_2\text{O}_3/\text{In}_2\text{S}_3$  nanostructures on FTO substrates. Corresponding to the previous reports, the color of  $\text{In}_2\text{S}_3$  is orange with band gap of 2.0-2.3 eV,<sup>48</sup> where  $\text{In}_2\text{O}_3$  reflects most of the visible light appearing almost white color.

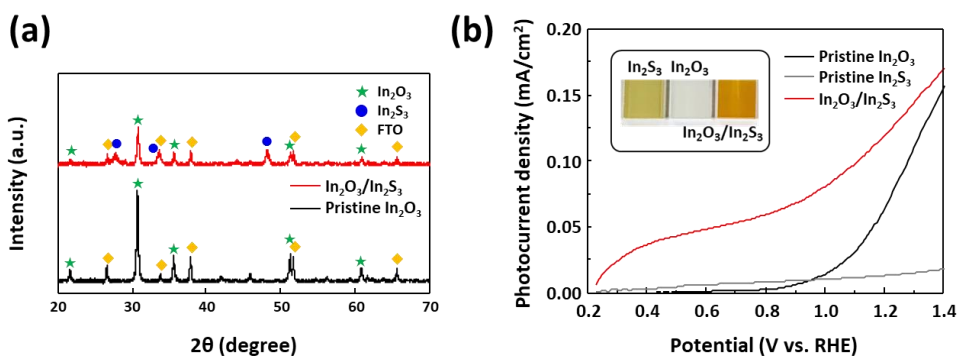


**Figure 3.2** (a) X-ray diffraction patterns of pristine  $\text{In}_2\text{O}_3$  and  $\text{In}_2\text{O}_3/\text{In}_2\text{S}_3$  photoanodes. (b) Linear sweep voltammograms of pristine  $\text{In}_2\text{O}_3$ , pristine  $\text{In}_2\text{S}_3$ , and  $\text{In}_2\text{O}_3/\text{In}_2\text{S}_3$ . Inset shows the photograph of pristine  $\text{In}_2\text{O}_3$ , pristine  $\text{In}_2\text{S}_3$ , and  $\text{In}_2\text{O}_3/\text{In}_2\text{S}_3$

To improve the PEC properties of the photoanodes, Co doping was conducted into the  $\text{In}_2\text{S}_3$  layer. By simply adding proper amount of  $\text{CoCl}_2$  precursor as Co source in the CBD reaction solution, Co ions were doped into  $\text{In}_2\text{S}_3$ . In the defect spinel lattice structure of  $\beta\text{-In}_2\text{S}_3$ , twelve tetrahedral sites are composed of eight occupied sites by  $\text{In}^{3+}$  ions and four empty sites.<sup>1</sup> Owing to the natural empty sites in its lattice, foreign metal ions can easily doped into  $\beta\text{-In}_2\text{S}_3$  at low synthesis temperatures.<sup>49</sup> TEM image of a single  $\text{In}_2\text{O}_3/\text{In}_2\text{S}_3$  nanorod, and its high-resolution TEM and selected area diffraction pattern are shown in Figure 3.3.  $\text{In}_2\text{S}_3$  layer were deposited with  $d$ -spacing of 0.39 nm, corresponding both to the (200) and (020) planes of cubic  $\beta\text{-In}_2\text{S}_3$ . Meanwhile, since the thickness of  $\text{In}_2\text{S}_3$  layer on the  $\text{In}_2\text{O}_3$  nanorods is over 100 nm, the signal from  $\text{In}_2\text{O}_3$  could not be detected. Also, there were no other patterns except for  $\text{In}_2\text{S}_3$ , indicating  $\text{Co}^{2+}$  doping rather than the formation of  $\text{CoS}_2$ . The existence of Co in the  $\text{In}_2\text{O}_3/\text{In}_2\text{S}_3$  heterostructures was demonstrated by the elemental mapping. Figure 3.4 shows the TEM Energy-dispersive X-ray spectroscopy (EDS) elemental maps of a single  $\text{In}_2\text{O}_3/\text{Co-In}_2\text{S}_3$  nanorod. According to Figure 3.4d and e,  $\text{In}_2\text{S}_3$  layer coated the  $\text{In}_2\text{O}_3$  nanorod conformally and Co ions were also distributed uniformly in the  $\text{In}_2\text{S}_3$  crystal structure.

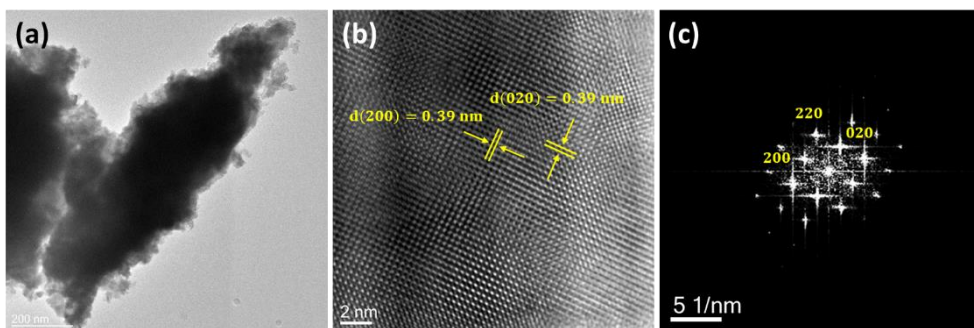


**Figure 3.3** (a) TEM image of a single  $\text{In}_2\text{O}_3/\text{Co-In}_2\text{S}_3$  nanorod. (b) High-resolution TEM and (c) selected area diffraction pattern showing crystalline plane of (200) and (020) of cubic  $\beta\text{-In}_2\text{S}_3$ .

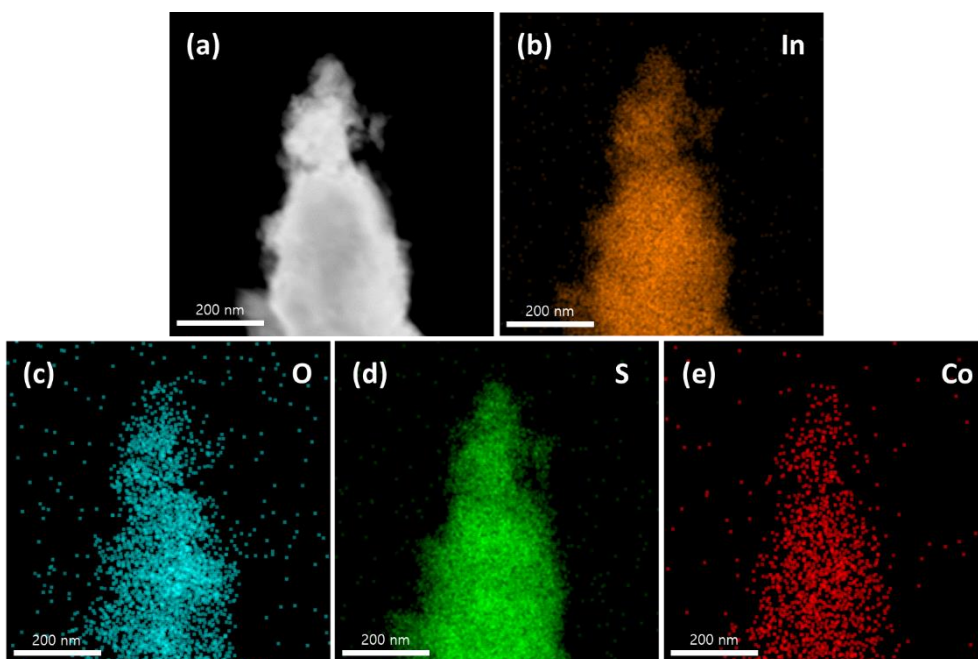


**Figure 3.4** (a) TEM image of a single  $\text{In}_2\text{O}_3/\text{Co-In}_2\text{S}_3$  nanorod and corresponding EDS element maps of (b) In, (c) O, (d) S, and (e) Co respectively.

PEC measurements were conducted to compare the  $\text{In}_2\text{O}_3/\text{In}_2\text{S}_3$  (IO/IS) photoanode and Co-doped  $\text{In}_2\text{O}_3/\text{In}_2\text{S}_3$  (IO/Co-IS) in 0.5 M  $\text{Na}_2\text{SO}_4$  solution under illumination. Figure 3.5a shows chopped linear sweep voltammograms of photoanodes with different amount of Co precursor in the reaction solution (3, 5, and 7 mol%). All of the doped samples showed the higher photocurrent density in the entire range of the applied voltages compared to the IO/IS. The photocurrent density of IO/Co-IS with 5 mol% of the precursor was 0.16  $\text{mA}/\text{cm}^2$  at 1.23 V vs. RHE which is 2.08 times and 1.26 times higher than that of pristine  $\text{In}_2\text{O}_3$  and as-prepared  $\text{In}_2\text{O}_3/\text{In}_2\text{S}_3$ , respectively. EIS spectra were collected in a frequency range of 100 KHz to 0.1 Hz with amplitude of 10 mV at 0.6 V vs. Ag/AgCl. The smaller diameter of arc for all IO/Co-IS nanostructures compared to that for IO/IS in the Nyquist plot (Figure 3.5b) indicates charge transfer resistance of the doped heterojunction photoanodes was decreased.<sup>2, 50-51</sup>

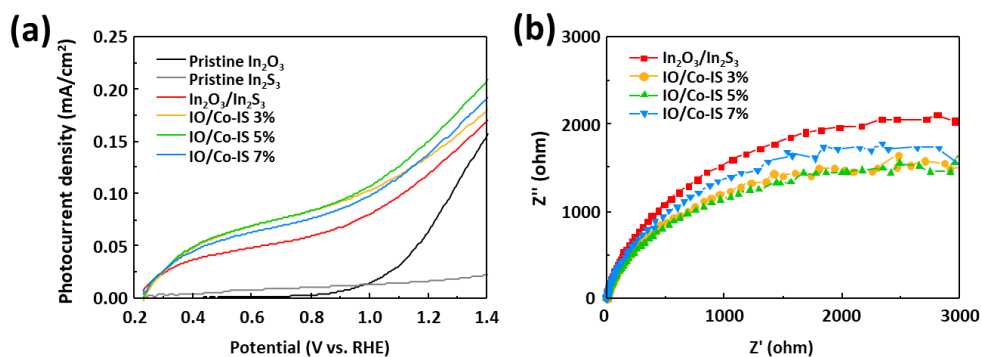


**Figure 3.5** (a) Linear sweep voltammograms of pristine In<sub>2</sub>O<sub>3</sub>, pristine In<sub>2</sub>S<sub>3</sub>, In<sub>2</sub>O<sub>3</sub>/In<sub>2</sub>S<sub>3</sub>, and In<sub>2</sub>O<sub>3</sub>/Co-In<sub>2</sub>S<sub>3</sub> with different amount of Co precursor concentration and (b) electrochemical impedance spectra of In<sub>2</sub>O<sub>3</sub>/In<sub>2</sub>S<sub>3</sub>, and In<sub>2</sub>O<sub>3</sub>/Co-In<sub>2</sub>S<sub>3</sub> with different amount of Co precursor concentration in 0.5 M Na<sub>2</sub>SO<sub>4</sub> solution under illumination.

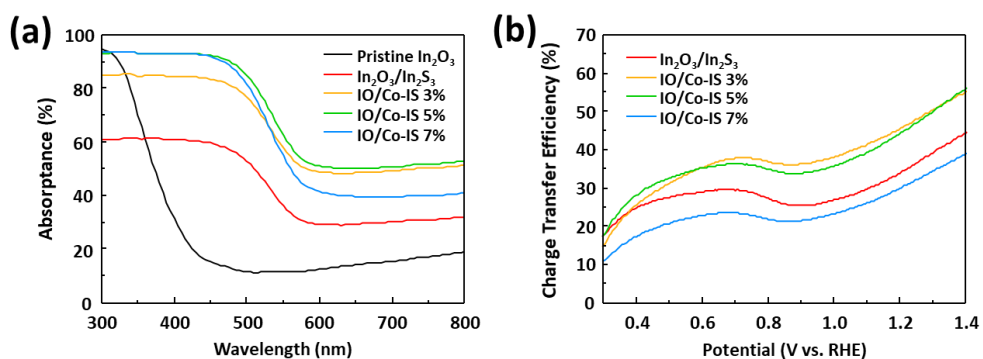


**Figure 3.6** (a) Absorbance spectra of pristine  $\text{In}_2\text{O}_3$ ,  $\text{In}_2\text{O}_3/\text{In}_2\text{S}_3$ , and  $\text{In}_2\text{O}_3/\text{Co-In}_2\text{S}_3$  with different amount of Co precursor concentration. (b) Charge transfer efficiency of  $\text{In}_2\text{O}_3/\text{In}_2\text{S}_3$  and  $\text{In}_2\text{O}_3/\text{Co-In}_2\text{S}_3$  with different amount of Co precursor concentration that was calculated by LSV data with and without using hole scavenger.

To further investigate the charge transfer property of the photoanodes, the charge transfer efficiency ( $\eta_{\text{trans}}$ ) was calculated by dividing the photocurrent density for water oxidation in  $\text{Na}_2\text{SO}_4$  solution by that for sulfite oxidation in  $\text{Na}_2\text{SO}_4/\text{Na}_2\text{SO}_3$  mixed solution ( $\eta_{\text{trans}} = J_{\text{H}_2\text{O}}/J_{\text{Na}_2\text{SO}_3}$ ). As shown in Figure 3.6a, the charge transfer efficiency of IO/Co-IS with 3 and 5 mol% was increased in the entire range of the applied voltages compared to that of IO/IS. According to the previous report, the surface area could be increased by doping Co into  $\text{In}_2\text{S}_3$  nanocrystal.<sup>1</sup> Thus, as the surface area increases by Co doping, the active sites were also increased for water oxidation, increasing the charge transfer efficiency. On the other hand, it is shown that IO/Co-IS with additional Co precursor over 5 mol% rather degraded the charge transfer property. That is, the excessive active sites came to be the recombination sites, hindering the charge transfer process.

The absorbance spectra of the prepared samples were collected by UV-vis transmission (T) and reflectance (R) spectroscopy (1-T-R). The absorption edge of the pristine  $\text{In}_2\text{O}_3$  photoanode was observed around 440 nm which corresponds to the band gap of  $\text{In}_2\text{O}_3$ . After constructing IO/IS heterostructures, the absorption edge was shifted positively indicating larger range of light including visible light can be harvested owing to the narrow band gap of  $\text{In}_2\text{S}_3$ . Interestingly, the absorbance was increased by Co doping into  $\text{In}_2\text{S}_3$  in the same range of wavelength. The improvement on light

harvesting by doping can be explained by increase of the surface area for efficient light absorption, which should be further demonstrated. To sum up, doping foreign metal ions into  $\beta$ - $\text{In}_2\text{S}_3$  enhanced PEC properties owing to the enlarged surface area and increased carrier density.

### **3.5. Conclusions**

In summary, we have successfully synthesized  $\text{In}_2\text{O}_3/\text{In}_2\text{S}_3$  heteronanostructures on FTO substrate by GLAD and CBD methods. The photocurrent density of  $\text{In}_2\text{S}_3$  was enhanced by constructing type II heterojunction and nanostructuring. Also, onset potential was shifted indicating the availability of low cost hydrogen production. Furthermore, doping Co ions into  $\text{In}_2\text{S}_3$  by a facile CBD process increased surface area and carrier density resulting in the enhanced charge transfer and light harvest ability. Further investigation on specific surface area and charge carrier density should be done. However, we demonstrated that doping Co into  $\text{In}_2\text{S}_3$  accelerated the charge transfer at the interface of electrode/electrolyte preventing the photocorrosion by hole accumulation on the surface of  $\text{In}_2\text{S}_3$ .

### 3.6. References

1. Pulipaka, S.; Koushik, A. K. S.; Deepa, M.; Meduri, P., Enhanced photoelectrochemical activity of Co-doped  $\beta$ - $\text{In}_2\text{S}_3$  nanoflakes as photoanodes for water splitting. *RSC Advances* **2019**, *9* (3), 1335-1340.
2. Wang, L.; Wang, W.; Chen, Y.; Yao, L.; Zhao, X.; Shi, H.; Cao, M.; Liang, Y., Heterogeneous p-n Junction CdS/Cu<sub>2</sub>O Nanorod Arrays: Synthesis and Superior Visible-Light-Driven Photoelectrochemical Performance for Hydrogen Evolution. *ACS Appl. Mater. Interfaces* **2018**, *10* (14), 11652-11662.
3. Baral, B.; Mansingh, S.; Reddy, K. H.; Bariki, R.; Parida, K., Architecting a Double Charge-Transfer Dynamics  $\text{In}_2\text{S}_3/\text{BiVO}_4$  n-n Iso-type Heterojunction for Superior Photocatalytic Oxytetracycline Hydrochloride Degradation and Water Oxidation Reaction: Unveiling the Association of Physicochemical, Electrochemical, and Photocatalytic Properties. *ACS Omega* **2020**, *5* (10), 5270-5284.
4. Huang, W.; Gan, L.; Yang, H.; Zhou, N.; Wang, R.; Wu, W.; Li, H.; Ma, Y.; Zeng, H.; Zhai, T., Controlled Synthesis of Ultrathin 2D  $\beta$ - $\text{In}_2\text{S}_3$  with Broadband Photoresponse by Chemical Vapor Deposition. *Advanced Functional Materials* **2017**, *27* (36).

5. Horani, F.; Lifshitz, E., Unraveling the Growth Mechanism Forming Stable  $\gamma$ - $\text{In}_2\text{S}_3$  and  $\beta$ - $\text{In}_2\text{S}_3$  Colloidal Nanoplatelets. *Chemistry of Materials* **2019**, *31* (5), 1784-1793.
6. Zhang, L.; Zhang, W.; Yang, H.; Fu, W.; Li, M.; Zhao, H.; Ma, J., Hydrothermal synthesis and photoelectrochemical properties of  $\text{In}_2\text{S}_3$  thin films with a wedgelike structure. *Applied Surface Science* **2012**, *258* (22), 9018-9024.
7. Tian, Y.; Wang, L.; Tang, H.; Zhou, W., Ultrathin two-dimensional  $\beta$ - $\text{In}_2\text{S}_3$  nanocrystals: oriented-attachment growth controlled by metal ions and photoelectrochemical properties. *Journal of Materials Chemistry A* **2015**, *3* (21), 11294-11301.
8. Xiong, Y.; Yang, L.; Nandakumar, D. K.; Yang, Y.; Dong, H.; Ji, X.; Xiao, P.; Tan, S. C., Highly efficient photoelectrochemical water oxidation enabled by enhanced interfacial interaction in 2D/1D  $\text{In}_2\text{S}_3$ @ $\text{Bi}_2\text{S}_3$  heterostructures. *Journal of Materials Chemistry A* **2020**, *8* (11), 5612-5621.
9. Li, H.; Chen, C.; Huang, X.; Leng, Y.; Hou, M.; Xiao, X.; Bao, J.; You, J.; Zhang, W.; Wang, Y.; Song, J.; Wang, Y.; Liu, Q.; Hope, G. A., Fabrication of  $\text{In}_2\text{O}_3$ @ $\text{In}_2\text{S}_3$  core-shell nanocubes for enhanced photoelectrochemical performance. *Journal of Power Sources* **2014**, *247*, 915-919.

10. Li, M.; Tu, X.; Wang, Y.; Su, Y.; Hu, J.; Cai, B.; Lu, J.; Yang, Z.; Zhang, Y., Highly Enhanced Visible-Light-Driven Photoelectrochemical Performance of ZnO-Modified In<sub>2</sub>S<sub>3</sub> Nanosheet Arrays by Atomic Layer Deposition. *Nanomicro Lett* **2018**, *10* (3), 45.
11. Sharma, M. D.; Mahala, C.; Basu, M., Photoelectrochemical Water Splitting by In<sub>2</sub>S<sub>3</sub>/In<sub>2</sub>O<sub>3</sub> Composite Nanopyramids. *ACS Applied Nano Materials* **2020**, *3* (11), 11638-11649.
12. Gao, Y.; Zhang, S.; Bu, X.; Tian, Y., Surface defect engineering via acid treatment improving photoelectrocatalysis of β-In<sub>2</sub>S<sub>3</sub> nanoplates for water splitting. *Catalysis Today* **2019**, *327*, 271-278.
13. Gao, C.; Li, J.; Shan, Z.; Huang, F.; Shen, H., Preparation and visible-light photocatalytic activity of In<sub>2</sub>S<sub>3</sub>/TiO<sub>2</sub> composite. *Materials Chemistry and Physics* **2010**, *122* (1), 183-187.
14. Sharma, R. K.; Chouryal, Y. N.; Chaudhari, S.; Saravanakumar, J.; Dey, S. R.; Ghosh, P., Adsorption-Driven Catalytic and Photocatalytic Activity of Phase Tuned In<sub>2</sub>S<sub>3</sub> Nanocrystals Synthesized via Ionic Liquids. *ACS Appl Mater Interfaces* **2017**, *9* (13), 11651-11661.
15. Rengaraj, S.; Venkataraj, S.; Tai, C. W.; Kim, Y.; Repo, E.; Sillanpaa, M., Self-assembled mesoporous hierarchical-like In<sub>2</sub>S<sub>3</sub> hollow microspheres composed of nanofibers and nanosheets and their photocatalytic activity. *Langmuir* **2011**, *27* (9), 5534-41.

16. Li, H.; Yuan, Z.; Bittencourt, C.; Li, X.; Li, W.; Chen, M.; Li, W.; Snyders, R., Anion exchange synthesis of hollow  $\beta$ - $\text{In}_2\text{S}_3$  nanoparticles: Adsorption and visible light photocatalytic performances. *Journal of Environmental Chemical Engineering* **2019**, 7 (1).
17. Xu, H.; Wang, Y.; Dong, X.; Zheng, N.; Ma, H.; Zhang, X., Fabrication of  $\text{In}_2\text{O}_3/\text{In}_2\text{S}_3$  microsphere heterostructures for efficient and stable photocatalytic nitrogen fixation. *Applied Catalysis B: Environmental* **2019**, 257.
18. Hua, E.; Jin, S.; Wang, X.; Ni, S.; Liu, G.; Xu, X., Ultrathin 2D type-II p-n heterojunctions  $\text{La}_2\text{Ti}_2\text{O}_7/\text{In}_2\text{S}_3$  with efficient charge separations and photocatalytic hydrogen evolution under visible light illumination. *Applied Catalysis B: Environmental* **2019**, 245, 733-742.
19. Dan, M.; Zhang, Q.; Yu, S.; Prakash, A.; Lin, Y.; Zhou, Y., Noble-metal-free  $\text{MnS}/\text{In}_2\text{S}_3$  composite as highly efficient visible light driven photocatalyst for  $\text{H}_2$  production from  $\text{H}_2\text{S}$ . *Applied Catalysis B: Environmental* **2017**, 217, 530-539.
20. Yao, Y.; Yin, M.; Yan, J.; Yang, D.; Liu, S., Controllable synthesis of  $\text{Ag}-\text{WO}_3$  core-shell nanospheres for light-enhanced gas sensors. *Sensors and Actuators B: Chemical* **2017**, 251, 583-589.
21. Omelianovych, A.; Kim, J. H.; Liudmila, L.; Ahn, B. T., Effect of post annealing on the characteristics of  $\text{In}_2\text{S}_3$  buffer layer grown by chemical

- bath deposition on a CIGS substrate. *Current Applied Physics* **2015**, *15* (12), 1641-1649.
22. Yuan, X.; Luo, Y.; Zhang, B.; Dong, C.; Lei, J.; Yi, F.; Duan, T.; Zhu, W.; He, R., Decoration of In nanoparticles on In<sub>2</sub>S<sub>3</sub> nanosheets enables efficient electrochemical reduction of CO<sub>2</sub>. *Chem Commun (Camb)* **2020**, *56* (30), 4212-4215.
23. Yang, J.; Zhu, X.; Mo, Z.; Yi, J.; Yan, J.; Deng, J.; Xu, Y.; She, Y.; Qian, J.; Xu, H.; Li, H., A multidimensional In<sub>2</sub>S<sub>3</sub>-CuInS<sub>2</sub> heterostructure for photocatalytic carbon dioxide reduction. *Inorganic Chemistry Frontiers* **2018**, *5* (12), 3163-3169.
24. Xue, B.; Xu, F.; Wang, B.; Dong, A., Shape-controlled synthesis of β-In<sub>2</sub>S<sub>3</sub> nanocrystals and their lithium storage properties. *CrystEngComm* **2016**, *18* (2), 250-256.
25. Lu, J.; Zheng, Z.; Gao, W.; Yao, J.; Zhao, Y.; Xiao, Y.; Wang, B.; Li, J., Epitaxial growth of large-scale In<sub>2</sub>S<sub>3</sub> nanoflakes and the construction of a high performance In<sub>2</sub>S<sub>3</sub>/Si photodetector. *Journal of Materials Chemistry C* **2019**, *7* (39), 12104-12113.
26. Xie, X.; Shen, G., Single-crystalline In<sub>2</sub>S<sub>3</sub> nanowire-based flexible visible-light photodetectors with an ultra-high photoresponse. *Nanoscale* **2015**, *7* (11), 5046-52.

27. Ma, H.; Zhang, J.; Liu, Z., Efficient tungsten oxide/bismuth oxyiodide core/shell photoanode for photoelectrochemical water splitting. *Applied Surface Science* **2017**, *423*, 63-70.
28. Lai, X.; Zhu, F.; Wu, Y.; Huang, R.; Wu, X.; Zhang, Q.; Yang, K.; Qin, S., New high-pressure polymorph of In<sub>2</sub>S<sub>3</sub> with defect Th<sub>3</sub>P<sub>4</sub>-type structure. *Journal of Solid State Chemistry* **2014**, *210* (1), 155-159.
29. Bayo ´n, R., Herrero, J., Structure and morphology of the indium hydroxy sulphide thin films. *Applied Surface Science* **2000**, *158*, 49-57.
30. Ma, B.; Yue, M.; Zhang, P.; Li, S.; Cong, R.; Gao, W.; Yang, T., Tetragonal  $\beta$ -In<sub>2</sub>S<sub>3</sub>: Partial ordering of In<sup>3+</sup> vacancy and visible-light photocatalytic activities in both water and nitrate reduction. *Catalysis Communications* **2017**, *88*, 18-21.
31. Jayakrishnan, R.; John, T. T.; Kartha, C. S.; Vijayakumar, K. P.; Jain, D.; Chandra, L. S. S.; Ganesan, V., Do the grain boundaries of  $\beta$ -In<sub>2</sub>S<sub>3</sub> thin films have a role in sub-band-gap photosensitivity to 632.8nm? *Journal of Applied Physics* **2008**, *103* (5).
32. Fu, X.; Wang, X.; Chen, Z.; Zhang, Z.; Li, Z.; Leung, D. Y. C.; Wu, L.; Fu, X., Photocatalytic performance of tetragonal and cubic  $\beta$ -In<sub>2</sub>S<sub>3</sub> for the water splitting under visible light irradiation. *Applied Catalysis B: Environmental* **2010**, *95* (3-4), 393-399.

33. Hsieh, P. Y.; Chiu, Y. H.; Lai, T. H.; Fang, M. J.; Wang, Y. T.; Hsu, Y. J., TiO<sub>2</sub> Nanowire-Supported Sulfide Hybrid Photocatalysts for Durable Solar Hydrogen Production. *ACS Appl Mater Interfaces* **2019**, *11* (3), 3006-3015.
34. Chen, D.; Liu, Z., Efficient Indium Sulfide Photoelectrode with Crystal Phase and Morphology Control for High-Performance Photoelectrochemical Water Splitting. *ACS Sustainable Chemistry & Engineering* **2018**, *6* (9), 12328-12336.
35. Zhao, Z.; Cao, Y.; Yi, J.; He, X.; Ma, C.; Qiu, J., Band-edge electronic structure of  $\beta$ -In<sub>2</sub>S<sub>3</sub>: the role of s or p orbitals of atoms at different lattice positions. *Chemphyschem* **2012**, *13* (6), 1551-6.
36. Pareek, A.; Paik, P.; Borse, P. H., Nanoniobia modification of CdS photoanode for an efficient and stable photoelectrochemical cell. *Langmuir* **2014**, *30* (51), 15540-9.
37. Lucena, R.; Fresno, F.; Conesa, J. C., Spectral response and stability of In<sub>2</sub>S<sub>3</sub> as visible light-active photocatalyst. *Catalysis Communications* **2012**, *20*, 1-5.
38. Wei, L.; Zhang, J.; Ruan, M., Combined CdS/In<sub>2</sub>S<sub>3</sub> heterostructures with cocatalyst for boosting carriers separation and photoelectrochemical water splitting. *Applied Surface Science* **2020**.

39. Kim do, H.; Andoshe, D. M.; Shim, Y. S.; Moon, C. W.; Sohn, W.; Choi, S.; Kim, T. L.; Lee, M.; Park, H.; Hong, K.; Kwon, K. C.; Suh, J. M.; Kim, J. S.; Lee, J. H.; Jang, H. W., Toward High-Performance Hematite Nanotube Photoanodes: Charge-Transfer Engineering at Heterointerfaces. *ACS Appl Mater Interfaces* **2016**, 8 (36), 23793-800.
40. Han, B. S.; Caliskan, S.; Sohn, W.; Kim, M.; Lee, J. K.; Jang, H. W., Room Temperature Deposition of Crystalline Nanoporous ZnO Nanostructures for Direct Use as Flexible DSSC Photoanode. *Nanoscale Res Lett* **2016**, 11 (1), 221.
41. Lee, B. R.; Lee, M. G.; Park, H.; Lee, T. H.; Lee, S. A.; Bhat, S. S. M.; Kim, C.; Lee, S.; Jang, H. W., All-Solution-Processed WO<sub>3</sub>/BiVO<sub>4</sub> Core-Shell Nanorod Arrays for Highly Stable Photoanodes. *ACS Appl Mater Interfaces* **2019**, 11 (22), 20004-20012.
42. Lahoucine Atourki, K. B., Ahmed Ihlal,; El hassane Ihalane, Y. A., Abdeslam; Elfanaoui, H. K., In<sub>2</sub>S<sub>3</sub> buffer layer prepared by chemical bath deposition. *2014 International Renewable and Sustainable Energy Conference (IRSEC)* **2014**, 85-88.
43. Pihosh, Y.; Turkevych, I.; Mawatari, K.; Uemura, J.; Kazoe, Y.; Kosar, S.; Makita, K.; Sugaya, T.; Matsui, T.; Fujita, D.; Tosa, M.; Kondo, M.; Kitamori, T., Photocatalytic generation of hydrogen by core-shell

- WO<sub>3</sub>/BiVO<sub>4</sub> nanorods with ultimate water splitting efficiency. *Sci Rep* **2015**, *5*, 11141.
44. Jeon, J.-M.; Shim, Y.-S.; Han, S. D.; Kim, D. H.; Kim, Y. H.; Kang, C.-Y.; Kim, J.-S.; Kim, M.; Jang, H. W., Vertically ordered SnO<sub>2</sub> nanobamboos for substantially improved detection of volatile reducing gases. *Journal of Materials Chemistry A* **2015**, *3* (35), 17939-17945.
45. Cho, I. S.; Han, H. S.; Logar, M.; Park, J.; Zheng, X., Enhancing Low-Bias Performance of Hematite Photoanodes for Solar Water Splitting by Simultaneous Reduction of Bulk, Interface, and Surface Recombination Pathways. *Advanced Energy Materials* **2016**, *6* (4).
46. Zheng, J.; Chang, F.; Jiao, M.; Xu, Q.; Deng, B.; Hu, X., A visible-light-driven heterojunctioned composite WO<sub>3</sub>/Bi<sub>12</sub>O<sub>17</sub>Cl<sub>2</sub>: Synthesis, characterization, and improved photocatalytic performance. *Journal of Colloid and Interface Science* **2018**, *510*, 20-31.
47. Yu-Jen Hsiao, C.-H. L., Liang-Wen Ji, Teen-Hang Meen, Yan-Lung Chen. Hsiao-Ping Chi, Characterization of photovoltaics with In<sub>2</sub>S<sub>3</sub> nanoflakes/p-Si heterojunction. *Nanoscale Research Letters* **2014**, (9), 32.
48. Jrad, F.; Naceur, J. B.; Ouertani, R.; Chtourou, R., Photo-electrochemical impedance spectroscopy analysis of hydrothermally

- synthesized  $\beta$ -In<sub>2</sub>S<sub>3</sub> thin film photo-anodes. *Physica E: Low-dimensional Systems and Nanostructures* **2019**, 114.
49. Zheng, Z.; Yu, J.; Cheng, S.; Lai, Y.; Zheng, Q.; Pan, D., Investigation of structural, optical and electrical properties of Cu doped  $\beta$ -In<sub>2</sub>S<sub>3</sub> thin films. *Journal of Materials Science: Materials in Electronics* **2016**, 27 (6), 5810-5817.
50. Musselman, K. P.; Marin, A.; Wisnet, A.; Scheu, C.; MacManus-Driscoll, J. L.; Schmidt-Mende, L., A Novel Buffering Technique for Aqueous Processing of Zinc Oxide Nanostructures and Interfaces, and Corresponding Improvement of Electrodeposited ZnO-Cu<sub>2</sub>O Photovoltaics. *Adv. Funct. Mater.* **2011**, 21 (3), 573-582.
51. Wang, Y.; Tian, W.; Chen, L.; Cao, F.; Guo, J.; Li, L., Three-Dimensional WO<sub>3</sub> Nanoplate/Bi<sub>2</sub>S<sub>3</sub> Nanorod Heterojunction as a Highly Efficient Photoanode for Improved Photoelectrochemical Water Splitting. *ACS Appl. Mater. Interfaces* **2017**, 9 (46), 40235-40243.

## 4. Conclusions

As the demand for sustainable energy increases, PEC water splitting using semiconductor materials has been extensively researched recently. This thesis covers the overall introduction of PEC water splitting including several critical factors that affect the PEC properties, several requirements for the semiconductor materials to be used as photoelectrodes and their limitations, and various strategies to overcome those limits and further enhance PEC properties.

First, all-solution-process was adopted to synthesis  $\text{WO}_3/\text{BiVO}_4$  core-shell heteronanostructures.  $\text{WO}_3$  nanorods were vertically grown on FTO substrates by facile hydrothermal method without seed layer. After that, pulsed-electrodeposition was performed to coat  $\text{BiVO}_4$  conformally on the  $\text{WO}_3$  nanorods array resulting in the formation of the  $\text{WO}_3/\text{BiVO}_4$  core-shell nanostructures. The optimized photoanode showed the high photocurrent density of  $4.15 \text{ mA/cm}^2$  which is double that of pristine  $\text{WO}_3$  nanorods. This is attributed to the increased charge transport efficiency by constructing type II heterojunction. Also, the photostability was far enhanced owing to the core-shell nanostructures.

Next,  $\beta\text{-In}_2\text{S}_3$ -based photoanodes were fabricated and studied. To achieve the large-area-film of  $\text{In}_2\text{S}_3$ ,  $\text{In}_2\text{O}_3$  nanorods were deposited by GLAD on FTO substrate first. After that,  $\text{In}_2\text{S}_3$  conformal layer was deposited by CBD on the

In<sub>2</sub>O<sub>3</sub> nanorods. Owing to the narrow band gap of In<sub>2</sub>S<sub>3</sub>, the on-set potential was negatively shifted. Also, the photocurrent density was enhanced due to the formation of heterojunction. To further improve the photostability, Co doping was successfully done by simply putting Co source in the CBD reaction solution. After Co doping, light harvesting was far improved and the charge transfer efficiency was increased, resulting in the higher photocurrent density.

In conclusion, since narrow-gap materials can harvest much more light but often suffer from photocorrosion and sluggish kinetics, some efforts should be contributed to overcome limitations and utilize them as photoanodes. Especially, nanostructuring and constructing type II heterostructures are essential for all semiconductor materials to achieve high photocurrent. Additionally, doping metal element would have an influence on light harvesting efficiency and charge transfer efficiency. By combining several strategies properly, the sustainable PEC water splitting technique would alternate the conventional energy production.

## 고효율 물분해 광전극 개발을 위한

### 금속 산화물 반도체 이종접합 나노구조체 합성 및 광전기화학적 특성 연구

전 세계의 에너지소비량이 증가함에 따라 지속 가능하고 친환경적인 에너지 개발 기술이 중요한 이슈로 떠오르고 있다. 광전기화학 물분해 기술은 태양에너지를 화학에너지로 직접 변환하는 기술로써 기존의 화석 연료를 대체할 수 있는 전도유망한 기술이다. 반도체 물질을 사용하여 효율적이고 안정한 물분해 광전극을 만들기 위해 수많은 노력이 있어왔지만 아직까지 이론값보다는 현저하게 낮은 에너지 변환 효율을 나타내고 있다. 따라서 기존에 널리 사용되었던 화석에너지를 대체하기 위해서는 더 많은 노력이 필요하다.

이 학위논문은 물분해 광전극에 대한 기초적인 이론을 소개하고 반도체 물질을 이용하여 효율적인 물분해 광전극을 제조하기 위한 여러가지 시도에 대한 이야기를 다룬다. 특히, 물의 산화 반응 속도가 전체 물분해 반응의 특성을 결정하기 때문에 산화 전극의 개발에 대해 논할 것이다. 먼저 제

1 장에서는 광전기화학 물분해 기술의 원리에 대해 설명하고 반도체 물질의 한계점을 극복하는 여러가지 방법에 대해 소개한다. 이중접합구조의 형성과 나노구조 제어는 효율적인 광전극을 제조하는데 있어서 가장 중요하고 필수적인 방법이다. 추가적으로 표면 안정화와 광촉매, 금속 이온 도핑 또한 광특성을 향상시키기에 효과적인 방법이다.

제 2 장에서는 전용액공정을 통한  $WO_3/BiVO_4$  이중접합 나노구조의 합성에 대해 소개한다. 지속 가능한 에너지 개발의 궁극적인 목표를 달성하기 위해 전극 제조과정 또한 지속 가능한 전용액공정을 통해 광전극을 개발하였다. 수열합성법을 이용하여  $WO_3$  나노막대를 FTO 기판에 수직으로 자라게 하였다. 여기에 펄스 기반의 전착법을 통해  $BiVO_4$  박막을 균일하게 코팅하였다. 최적화 된 샘플의 경우  $WO_3$  단일 물질 전극과 비교하여 두 배 이상의 전류 밀도를 보였으며 광 안정성도 눈에 띄게 증가하였다. 이러한 물분해 특성의 향상은 제조된 나노구조가 core-shell 구조를 나타내기 때문이라고 할 수 있다. 펄스 기반의 전착법을 통해 아주 얇고 균일한  $BiVO_4$  박막을  $WO_3$  나노막대 위에 코팅함으로써 전극과 전해질의 계면에서의 전하 전달 특성과 전극 물질 내의 전하 분리가 용이해졌다. 또한 core-shell 나노구조로 인해 일반적인  $BiVO_4$  기반 광전극과 다르게

전면에서 빛을 비추었을 때의 전류밀도가 더 높아 상용화 가능성이 더욱 높아졌다.

제 3 장에서는 베타 상의 입방체  $\text{In}_2\text{S}_3$  기반 광전극을 소개한다.  $\text{In}_2\text{S}_3$  는 약 2.1 eV 의 밴드갭을 가진다.  $\text{In}_2\text{S}_3$  의 특이한 결정구조로 인해 생기는 여러가지 이점 덕분에 광반응 물질로서 최근 재조명되었다.  $\text{In}_2\text{S}_3$  기반 광전극의 광전기화학 특성을 향상시키기위해 여러가지 방법을 결합해보았다. 먼저 glancing angle deposition 을 통해  $\text{In}_2\text{O}_3$  나노막대를 만들고 그 위에 화학용액증착법을 통해  $\text{In}_2\text{S}_3$  박막을 합성하여 이종접합을 형성한 결과 광전류밀도가 증가하였고 onset 전위가 낮아졌다. 여기에 코발트 전구체를 반응 용액에 추가하여 화학용액증착법을 진행함으로써  $\text{In}_2\text{S}_3$  결정 내에 코발트 이온을 도핑하였다. 도핑 농도를 조절하여 합성한 나노구조체는 빛 흡수 효율과 전하 전달 효율이 증가하였고 이는 정공이 전극의 표면에 쌓이는 것을 막아주기 때문에  $\text{In}_2\text{S}_3$  기반 광전극의 광전류밀도 뿐만 아니라 광 안정성까지도 증가하였다.

**키워드:** 광전기화학, 물분해, 이종접합구조, Core-shell, 광안정성